

Joint Hardware Design and Capacity Analysis for Intelligent Reflecting Surface Enabled Terahertz MIMO Communications

Xinying Ma, Zhi Chen, Wenjie Chen, Yaojia Chi, Longfei Yan,
Chong Han, and Shaoqiana Li

Abstract

Terahertz (THz) communications have been envisioned as a promising enabler to provide ultra-high data transmission for sixth generation (6G) wireless networks. To tackle the blockage vulnerability brought by severe path attenuation and poor diffraction of THz waves, an intelligent reflecting surface (IRS) is put forward to smartly control the incident THz waves by adjusting the phase shifts. In this paper, we firstly design an efficient hardware structure of graphene-based IRS with phase response up to 306.82 degrees. Subsequently, to characterize the capacity of the IRS-enabled THz multiple-input multiple-output (MIMO) system, an adaptive gradient descent (A-GD) algorithm is developed by dynamically updating the step size during the iterative process, which is determined by the second-order Taylor expansion formulation. In contrast with conventional gradient descent (C-GD) algorithm with fixed step size, the A-GD algorithm evidently improves the achievable rate performance. However, both A-GD algorithm and C-GD algorithm inherit the unacceptable complexity. Then a low complexity alternating optimization (AO) algorithm is proposed by alternately optimizing the precoding matrix by a column-by-column (CBC) algorithm and the phase shift matrix of the IRS by a linear search algorithm. Ultimately, the numerical results demonstrate the effectiveness of the designed hardware structure and the considered algorithms.

Index Terms

Terahertz (THz) communications, intelligent reflecting surface (IRS), capacity analysis, adaptive gradient descent (A-GD), alternating optimization (AO).

I. INTRODUCTION

With the continuous explosion growth of data traffic in wireless communications, sixth generation (6G) communication networks are expected to meet a great deal of pressing requirements

in the near future, such as increased spectral efficiency, higher data rate, lower latency, larger connection density and so on [1], [2]. To settle these challenges, Terahertz (THz) frequency band (0.1-10 THz) has been regarded as a prospective alternative to provide large spectrum bandwidth and support ultra-high data transmission for 6G communication networks [3]. Since THz communication is able to realize high transmission rates from hundreds of gigabits per second (Gbps) to several terabits per second (Tbps), some typical application scenarios are defined and considered recently, including intra-device communications, high speed kiosk downloads, wireless data centers and wireless backhaul networks [4]. From the perspective of spectrum resources, THz frequency band bridges the gap between millimeter wave (mmWave) and optical frequency ranges [5]. Compared with mmWave frequency band, THz communication possesses much larger bandwidth and better security performance. In contrast with optical frequency band, THz communication is much easier to realize the beam tracking, and adapts inconvenient climate conditions. Enabled by these obvious advantages, THz communication is regarded as an indispensable technology for 6G communication networks.

Despite the numerous advantages, there are still some imperative challenges existing in THz communication systems. On the one hand, due to the high path attenuation and strong molecular absorption effect experienced by THz waves, the transmission distance of THz communications is limited within a small area, and thus is applicable for the specific communication scenarios [6], [7]. On the other hand, THz waves at such a high frequency band undergo extremely poor diffraction, and THz communication links that depend on the line-of-sight (LOS) path are easily blocked by the obstacles. Given this, a concept of an intelligent reflecting surface (IRS) is newly proposed to mitigate blockage vulnerability and improve coverage capability [8]–[10]. To be specific, an IRS is a kind of physical meta-surface consisting of a large number of passive reflecting elements. Each reflecting element is capable of adjusting the phase shifts by using a smart processor. One may note that an IRS is composed of passive reflecting elements without any active radio frequency (RF) chains, and thus the hardware complexity and power consumption of the IRS-enabled THz communication system are much lower than conventional solutions (e.g., reflect array, relaying, backscatter communication) [9]. Therefore, the IRS-enabled THz communication systems are worthy of further exploration.

Although deploying an IRS in the THz communication system is essential, some challenges also emerge accordingly. To realize reliable THz communications, the channel state information (CSI) acquisition is the primary mission before the data transmission begins. Different from

conventional communication systems with active devices, the main difficulty of channel estimation problem in IRS-enabled THz systems is that the reflecting elements are passive and are unable to achieve the signal processing. Prominently, by leveraging the sparse features (e.g., sparsity, path loss) of THz multiple-input multiple-output (MIMO) channel, the authors convert the channel estimation problem into the sparse signal recovery problem, and a low complexity compressed sensing (CS) based channel estimation scheme is developed to realize the efficient signal reconstruction [11]. Once the CSI is acquired at the base station (BS) side or the mobile station (MS) side, the extensive research directions can be investigated, such as energy efficiency optimization [10], data rate maximization [12], [13], secure communication [14]. Apart from these research interests mentioned above, the capacity analysis for the IRS-enabled MIMO communication system is still treated as an open problem.

In order to compensate for the research gap, the joint hardware design and capacity characterization of the IRS-enabled THz MIMO system is presented in this paper. To the best of our knowledge, *this paper is the first attempt to settle the achievable rate optimization problem at THz band and to practically combine the hardware characteristic with software design together.* Firstly, we design an efficient graphene-based hardware structure of each IRS elements with a wide phase response range and a desired reflecting amplitude. With the given hardware foundation, a downlink IRS-enabled THz MIMO communication system model is developed. Then, in the software design part, the gradient descent based algorithm and the alternating optimization (AO) algorithm are put forward to jointly optimize the phase shift matrix at the IRS and the hybrid beamforming matrix at the BS, which greatly differs from the previous work in [15] that only considers the phase shift design of the IRS. Compared with the conventional MIMO system without the IRS [16], [17], such a capacity characterization problem of the IRS-enabled THz MIMO system involves multiple matrix variables, and thus is more sophisticated. The main contributions of this paper can be summarized as follows.

- **To begin with, an efficient hardware structure of the graphene-based IRS is designed with the phase response range up to 306.82 degrees and the reflecting amplitude efficiency more than 50%.** In the section of hardware preliminaries, the design theory and working principle of the IRS are explained firstly. Then, the electric properties of the graphene are introduced by revealing the relationship between conductivity and applied voltage, which is the foundation of forming an electrically-controlled IRS. Based on the graphene properties, the hardware structure of each IRS element is designed according to

Fabry-Perot resonance model. In terms of each reflecting element, we present simulation results of the phase response and the reflecting amplitude. In addition, the hardware design of the whole IRS is accomplished, including the element arrangement, size selection in various situations and discrete phase distribution for a simplified hardware structure.

- **Next, the adaptive gradient descent (A-GD) algorithm and the conventional gradient descent (C-GD) algorithm are developed to seek a high-quality solution of the capacity characterization problem existing in the IRS-enabled THz MIMO system.** To deal with the phase shift matrix optimization of the IRS, the A-GD algorithm turns out to be more efficient by dynamically updating the step size during the iterative process compared with C-GD algorithm with fixed step size. More importantly, the adaptive step size of the A-GD algorithm is determined by the coefficients of second-order Taylor expansion formulation, and thus the developed A-GD algorithm is able to realize a better achievable rate performance of the IRS-enabled THz MIMO system.
- **Moreover, to combat the intolerable complexity brought by the C-GD algorithm and the A-GD algorithm, a low complexity AO algorithm is raised to settle the achievable rate maximization problem by alternately optimizing the precoding matrix and the phase shift matrix of the IRS.** On the one hand, a column-by-column (CBC) algorithm is proposed to solve the precoding matrix by decomposing the hybrid beamforming problem into a column-form. Then we derive the closed-form solution for obtaining the analog and digital beamforming matrices separately. On the other hand, in order to determine the phase shift matrix of the IRS, a linear search algorithm is considered by utilizing the one-the-rest criterion. In detail, the one-the-rest criterion indicates that only one reflecting coefficient of these IRS elements is variable while the rest elements remain fixed.

The reminder of this paper is organized as follows. In Section II, a novel hardware structure of graphene-based IRS is designed. In Section III, the system model and the channel model of the IRS-enabled THz MIMO system are described in detail. Section IV proposes two different gradient descent algorithms (e.g., A-GD, C-GD). Then, an AO algorithm is introduced by alternately operating the CBC scheme and the linear search scheme in Section V. Subsequently, the simulation results and the conclusion are presented in Section VI and Section VII, respectively.

Notations: \mathbf{A} is a matrix, \mathbf{a} is a vector, a is a scalar. $\|\mathbf{A}\|_F$ is the Frobenius norm, whereas \mathbf{A}^H , \mathbf{A}^* , \mathbf{A}^T , \mathbf{A}^{-1} , \mathbf{A}^\dagger , $|\mathbf{A}|$ and $rank(\mathbf{A})$ are conjugate transpose, conjugate, transpose, inverse, pseudo-inverse, determinant and the rank of \mathbf{A} , respectively. $\text{diag}(\mathbf{a})$ is a diagonal matrix with

elements of \mathbf{a} on its diagonal. $\text{Tr}(\mathbf{A})$ is the trace of matrix \mathbf{A} . $\mathbb{E}[\cdot]$ is used to denote the expectation. $\text{vec}(\mathbf{A})$ is the column-ordered vectorization of matrix \mathbf{A} , and $\text{vec}^{-1}(\mathbf{A})$ is the reverse operation of $\text{vec}(\mathbf{A})$. $\mathcal{O}(\cdot)$ indicates the number of complex multiplications.

II. GRAPHENE ENABLED INTELLGENT REFLECTING SURFACE DESIGN

The IRS is an artificial planar structure that is widely utilized to control and manipulate electromagnetic (EM) waves [18]. The key component of an IRS is the reflecting elements with sub-wavelength thickness, and each element needs to be designed as a tunable resonant structure. With the shifting of resonant state, the effective refraction index (an important factor to the propagation of EM waves through IRS) of each reflecting element is tailored. Meanwhile, the reflecting amplitude and the phase response are obtained correspondingly. By arranging these reflecting elements in a specific way, the whole IRS array is capable of realizing diverse functions, such as phase control, anomalous reflection, planar focusing and so on. In this section, a novel graphene-based IRS is designed and simulated to assist the THz communications. Additionally, the detailed working principle and device performance is also presented in the following.

A. Electric Properties of Graphene at THz Band

As discussed above, the IRS is composed of passive reflecting elements that dynamically controls the direction of incident EM waves. In order to achieve the beam controllability, tunable components are embedded into the IRS elements. In general, semiconductor devices are extensively utilized at microwave frequency band like varactor diode and switching diode. Nevertheless, the physical size of each reflecting element at THz band is much tinier so that diodes and transistors can not be integrated into such a structure. In this case, graphene is a kind of appropriate material to facilitate the IRS with ultra-small size and tunable property.

Graphene is a two-dimensional material consisting of a single layer of carbon atoms. The conductivity of graphene can be altered through voltage bias in a relatively wide range, and therefore graphene provides various resonant states for each IRS element. According to [19], the conductivity of graphene at THz band can be written as

$$\sigma = \frac{2e^2}{\pi\hbar^2} k_B T \cdot \ln \left[2 \cosh \left(\frac{E_F}{2k_B T} \right) \right] \frac{i}{\omega + i\tau^{-1}}, \quad (1)$$

where e is the elementary charge, \hbar is the reduced Planck constant, k_B is the Boltzmann constant, T is the temperature, E_F is the Fermi level, τ is the relaxation time and ω is the angular

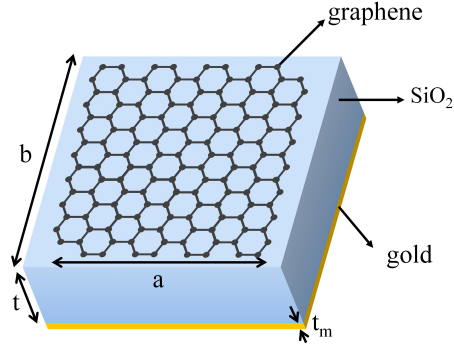


Fig. 1: Illustration of an IRS element that consists of graphene, quartz (substrate) and gold (ground plane) with $a = 66\mu\text{m}$, $b = 70\mu\text{m}$, $t = 38\mu\text{m}$ and $t_m = 1\mu\text{m}$.

frequency, respectively. It can be concluded that at a certain frequency point, the conductivity is only determined by Fermi level [20]. Then we can get the following expression as

$$|E_F| = \hbar\nu_F\sqrt{\pi n_d}, \quad (2)$$

where ν_F is the Fermi velocity and n_d is the carrier density which can be expressed as V_g [21]

$$n_d = \sqrt{n_0^2 + \alpha|V_{\text{CNP}} - V_g|^2}, \quad (3)$$

where n_0 is the residual carrier density, α is capacitivity related to the electrode, V_{CNP} is the compensating voltage. In summary, the conductivity of graphene can be continuously changed by the applied voltages, which is the foundation of forming an electrically controlled IRS.

B. Hardware Design of Graphene Based IRS

The EM responses of the reflecting elements play an important role in the hardware structure of the IRS. Fig. 1 shows a typical hardware design of an IRS element, which can be divided into three parts from top to the bottom: the graphene layer, the substrate and the metallic ground plane. The resonance model of this IRS architecture can be described as a Fabry-Perot cavity, where EM waves reflect back and forth between the top and the bottom surfaces. In addition, the resonance responses are caused by constructive or destructive interference of the multiple reflections [22]. In terms of such a reflecting element structure as shown in Fig. 1, the reflecting phase response based on [23] can be expressed as

$$\varphi = m\pi - ak_0\text{Re}(n_{eff}), \quad (4)$$

where m is an integer, a is the width of graphene patch, k_0 is the wave number of free space, and n_{eff} is the effective refraction index of the resonant structure, which is related to the effective permittivity ε_{eff} of the graphene. In light of [24], the parameter ε_{eff} can be written as

$$\varepsilon_{eff} = 1 + \frac{i\sigma}{\omega\varepsilon_0 t_g}, \quad (5)$$

where σ is the conductivity and t_g denotes the thickness of graphene. Combining (4) and (5), the phase response can be altered by the conductivity of graphene as well as the applied voltages.

The reflecting elements are simulated by leveraging the frequency domain solver in the simulation environment of CST Microwave Studio 2016. It is worth noting that a single reflecting element is unable to work since the miniature size causes the strong scattering. As a result, the boundary condition of the IRS is set as ‘unit cell’ to mimic the repeated arrangement of the IRS elements. Notably, the reflecting coefficient for each IRS element is composed of reflecting amplitude and phase shift. Fig.2 illustrates the simulation results of the reflecting coefficient from 1.4 THz to 1.8 THz with various Fermi levels. By combining Fig. 2 (a) and Fig. 2 (b), our designed IRS element performs relatively stable broadband characteristics. However, a narrowband working mode of the IRS elements is selected in this paper where the center frequency is located at 1.6 THz. Fig. 2 (c) verifies that the amplitude efficiency of our designed reflecting element at 1.6 THz is more than 50%. Meanwhile, as shown in Fig.2 (c), the phase response range of our proposed hardware structure at 1.6 THz reaches to 306.82 degrees with the chemical potential of graphene ranging from 0 eV to 2 eV. Except for the wide phase response range, the discrete phase shifts at 1.6 THz are also well-distributed with diverse Fermi levels.

Once the hardware design of a single IRS element is accomplished, the following target is to arrange massive reflecting elements closely in an array structure, as shown in Fig. 3. In our simulation environment, we need to take the limitation of computer memory into consideration, and thus the side length of the whole array is usually set as $5\bar{\lambda} \sim 10\bar{\lambda}$ (where $\bar{\lambda}$ is the incident wavelength) to avoid the wave scattering. But in practice, the real size of the IRS is dependent on the THz beam width that can fully cover the incident waves.

Various functions can be realized by controlling the phase response of the IRS elements, and phase control is one of the fundamental functions of an IRS, as shown in Fig. 3. Also, the phase control function demands all the reflecting elements to have the equal phase responses. According to the simulation results in Fig.2 (c), any expected phase shift within the phase response range $[0^\circ, 306.82^\circ]$ can be obtained via applying the voltages continuously. However,

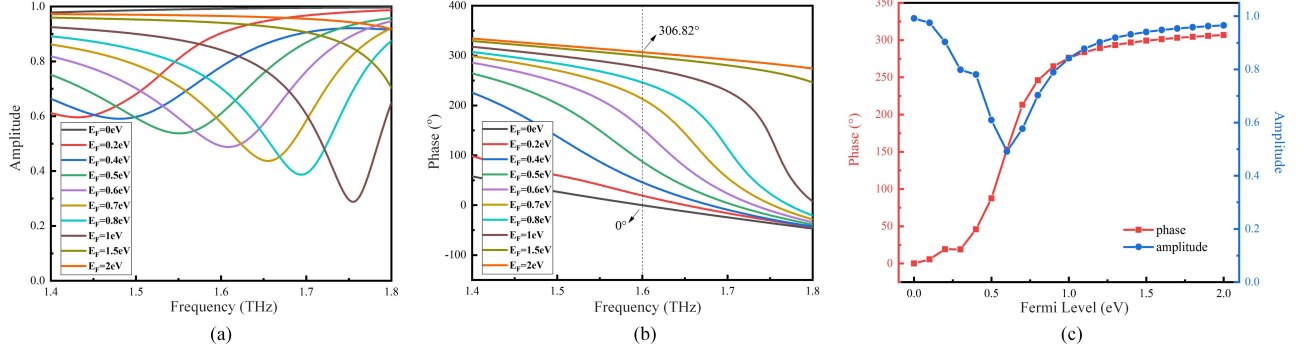


Fig. 2: Simulation results of the reflecting coefficient: (a) The response of reflecting amplitude; (b) The response of phase shift; (c) Phase response and reflecting amplitude versus Fermi level at 1.6 THz, where the phase response is $[0^\circ, 306.82^\circ]$ with reflecting amplitude more than 50%.

the continuous phase control for each IRS element results in extremely high hardware complexity and heavy system consumption in practice. To this end, an IRS with discrete phase shifts is considered in this paper to simplify the hardware structure. For example, we assume that the phase response range is $[0, \varphi_{\max}]$, the phase shift of each reflecting element belongs to the phase set $\mathcal{F} = \{0, \varphi_{\max}/2^b, \dots, (2^b - 1)\varphi_{\max}/2^b\}$, where φ_{\max} is the maximum phase response and b is the bit quantization number. Apart from the phase response, the reflecting amplitude is also an essential parameter for each IRS element. From Fig.2 (c) we can note that a phase shift corresponds to a distinctive reflecting amplitude. In other words, when the distribution of the phase shifts is determined, the reflecting amplitude set can be acquired accordingly. Here, the reflecting amplitude set is defined as $\mathcal{A} = \{\mu_1, \dots, \mu_{|\mathcal{F}|}\}$, where $|\mathcal{F}| = 2^b$. To simplify the optimization problem, we focus on optimizing the phase shifts and redefine the influence of amplitude variation. Thus, the reflecting amplitude for each reflecting element can be further defined as $\bar{\mu} = \left(\sum_{i=1}^{|\mathcal{F}|} \mu_i\right) / |\mathcal{F}|$, where the averaged amplitude $\bar{\mu} \in [0.5, 1]$ is determined by the bit quantization number b and the considered hardware structure of an IRS.

III. SYSTEM MODEL AND CHANNEL MODEL

A. System Model

Considering a downlink THz MIMO communication system as shown in Fig. 4, a BS employs N_{BS} antennas to serve a MS equipped with N_{MS} antennas. Since the LOS path between the BS and the MS is usually blocked by the obstacles, we suppose that our developed IRS is installed in

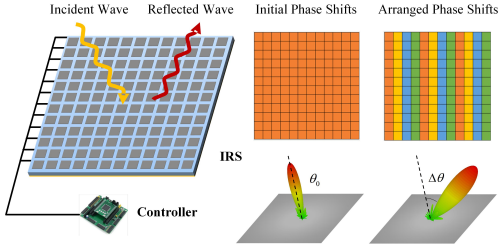


Fig. 3: Hardware design of the IRS. Various phase distributions are represented by different color blocks.

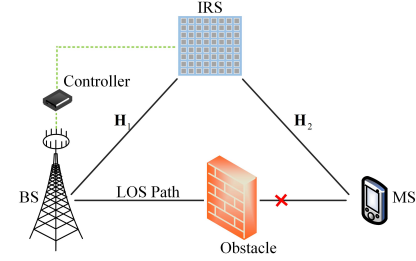


Fig. 4: Illustration of the IRS-enabled THz MIMO communication system.

to assist this communication link, which consists of N_{IRS} passive reflecting elements. The phase shift of each reflecting element can be selected from the phase set \mathcal{F} . Considering the high path loss of THz waves, the THz signals are reflected by the IRS for the first time is considered, and the NLOS paths that are reflected more than one time are ignored. In addition, a controller that connects the BS and the IRS is also required to realize the phase adjustment. Also, we assume there are M_{BS} RF chains at BS side, and M_{MS} RF chains at MS side. Due to the serious power consumption of the RF circuits, the number of antennas is larger than the number of the RF chains, i.e. $N_{\text{BS}} > M_{\text{BS}}$, $N_{\text{MS}} > M_{\text{MS}}$. When the BS sends N_s data streams $\mathbf{s} \in \mathbb{C}^{N_s \times 1}$, the MS employs M_{MS} RF chains to receive the processed signals. Thus, the received signal $\mathbf{y}_r \in \mathbb{C}^{N_s \times 1}$ can be expressed as

$$\mathbf{y}_r = \sqrt{\rho} \mathbf{W}_{\text{BB}}^H \mathbf{W}_{\text{RF}}^H \mathbf{H}_2 \mathbf{\Phi} \mathbf{H}_1 \mathbf{F}_{\text{RF}} \mathbf{F}_{\text{BS}} \mathbf{s} + \mathbf{W}_{\text{BB}}^H \mathbf{W}_{\text{RF}}^H \mathbf{n}, \quad (6)$$

where ρ is the transmission power, $\mathbf{H}_1 \in \mathbb{C}^{N_{\text{IRS}} \times N_{\text{BS}}}$ indicates BS-IRS channel, $\mathbf{H}_2 \in \mathbb{C}^{N_{\text{MS}} \times N_{\text{IRS}}}$ indicates IRS-MS channel, $\mathbf{F}_{\text{RF}} \in \mathbb{C}^{N_{\text{BS}} \times M_{\text{BS}}}$ ($\mathbf{F}_{\text{BB}} \in \mathbb{C}^{M_{\text{BS}} \times N_s}$) denotes the analog (digital) precoding matrix, $\mathbf{W}_{\text{RF}} \in \mathbb{C}^{N_{\text{MS}} \times M_{\text{MS}}}$ ($\mathbf{W}_{\text{BB}} \in \mathbb{C}^{M_{\text{MS}} \times N_s}$) denotes the analog (digital) combining matrix, $\mathbf{n} \in \mathbb{C}^{N_{\text{MS}} \times 1}$ represents the additive white Gaussian noise (AWGN) vector following the distribution of $\mathbb{CN}(0, \delta^2)$ and $\mathbf{\Phi} = \text{diag}(\bar{\mu}e^{j\varphi_1}, \bar{\mu}e^{j\varphi_2}, \dots, \bar{\mu}e^{j\varphi_{N_{\text{IRS}}}})$ is a diagonal matrix with the dimension of $N_{\text{IRS}} \times N_{\text{IRS}}$, respectively. Each entry $\{\bar{\mu}e^{j\varphi_i}\}_{i=1}^{N_{\text{IRS}}}$ of the phase shift matrix $\mathbf{\Phi}$ indicates the reflecting coefficient of an IRS element, which is composed of the reflecting amplitude $\bar{\mu}$ and the phase shift $\{\varphi_i\}_{i=1}^{N_{\text{IRS}}}$. Moreover, $\bar{\mu}$ is treated as a constant while $\mathbf{\Phi}$ is a matrix variable during the capacity analysis process.

B. Channel Model

The IRS-enabled THz MIMO channel model contains \mathbf{H}_1 , Φ and \mathbf{H}_2 , and the cascaded channel is denoted as $\mathbf{H}_e = \mathbf{H}_2 \Phi \mathbf{H}_1$. Without loss of generality, we assume that both \mathbf{H}_1 and \mathbf{H}_2 consist of a LOS path and several NLOS paths, as we take the sparse nature of the THz channel into consideration. On the basis of geometric channel model [25], \mathbf{H}_1 can be written as

$$\begin{aligned} \mathbf{H}_1 = & \sqrt{N_{\text{BS}} N_{\text{IRS}}} \alpha_0 G_t G_r \mathbf{a}_{\text{IRS}}(\theta_{\text{IRS},0}^1, \theta_{\text{IRS},0}^2) \mathbf{a}_{\text{BS}}^H(\theta_{\text{BS},0}^1, \theta_{\text{BS},0}^2) \\ & + \sqrt{\frac{N_{\text{BS}} N_{\text{IRS}}}{L}} \sum_{l=1}^L \alpha_l G_t G_r \mathbf{a}_{\text{IRS}}(\theta_{\text{IRS},l}^1, \theta_{\text{IRS},l}^2) \mathbf{a}_{\text{BS}}^H(\theta_{\text{BS},l}^1, \theta_{\text{BS},l}^2), \end{aligned} \quad (7)$$

where L is the number of NLOS paths, G_t is the transmitting antenna gain, G_r is the receiving antenna gain, θ_{IRS}^1 (θ_{IRS}^2) denotes the angle of arrival (AoA) of \mathbf{H}_1 in the azimuth (elevation) domain, θ_{BS}^1 (θ_{BS}^2) denotes the angles of departure (AoD) of \mathbf{H}_1 in the azimuth (elevation) domain, respectively. Considering the large number of THz array antennas, the uniform planar array (UPA) structure is adopted as the array geometry. The normalized array response for the UPA with $N_x N_y$ -elements, in which N_x and N_y elements are placed on the x -axis and y -axis, can be expressed as

$$\begin{aligned} \mathbf{a}_{\text{BS}}(\theta_{\text{BS}}^1, \theta_{\text{BS}}^2) = & \frac{1}{\sqrt{N_{\text{BS}}}} [1, \dots, e^{j2\pi d[p \sin(\theta_{\text{BS}}^2) \cos(\theta_{\text{BS}}^1) + q \sin(\theta_{\text{BS}}^2) \sin(\theta_{\text{BS}}^1)]/\lambda}, \\ & \dots, e^{j2\pi d[N_x \sin(\theta_{\text{BS}}^2) \cos(\theta_{\text{BS}}^1) + N_y \sin(\theta_{\text{BS}}^2) \sin(\theta_{\text{BS}}^1)]/\lambda}]^T, \end{aligned} \quad (8)$$

where $p \in [1, N_x]$, $q \in [1, N_y]$, $N_x N_y = N_{\text{BS}}$, d is the THz antenna spacing and equals to half wavelength $\bar{\lambda}/2$ of incident waves. Similar to (8), $\mathbf{a}_{\text{IRS}}(\theta_{\text{IRS}}^1, \theta_{\text{IRS}}^2)$ also employs the UPA structure. However, different from the array antennas, the spacing of the IRS elements is the side length of each reflecting element. In addition, α_0 is the LOS path gain of \mathbf{H}_1 . As discussed in [26], α_0 consists of the spreading loss $\alpha_{\text{Spr}}(f)$ and the molecular absorbing loss $\alpha_{\text{Abs}}(f)$, which can be formulated as

$$\alpha_0 = \alpha_{\text{Spr}}(f) \cdot \alpha_{\text{Abs}}(f) \cdot e^{-j2\pi f \tau_{\text{Los}}} = \frac{c}{4\pi f r} \cdot e^{-\frac{1}{2}\kappa(f)r} \cdot e^{-j2\pi f \tau_{\text{Los}}}, \quad (9)$$

where c is the speed of light, r_0 is the straight distance between the BS and the MS, $\tau_{\text{Los}} = r/c$ is the time-of-arrival of the LOS path, $\kappa(f)$ is the coefficient of the molecular absorbing loss and is determined by f . In addition, the channel gain α_l for the l th reflected path based on [26] can be written as

$$\alpha_l = \frac{c}{4\pi f (r_1 + r_2)} \cdot e^{-\frac{1}{2}\kappa(f)(r_1 + r_2)} \cdot e^{-j2\pi f \tau_{\text{Ref}}} \cdot \xi(f), \quad (10)$$

where $\xi(f)$ is the reflection coefficient of the reflecting materials (e.g., concrete, plastic, glass), r_1 is the distance between the transmitter and the reflecting material, r_2 is the distance between the receiver and the reflecting material, and $\tau_{\text{Ref}} = \tau_{\text{Los}} + (r_1 + r_2 - r)/c$ is the time-of-arrival of the reflected path. Besides, the channel characteristics of \mathbf{H}_2 are identical to \mathbf{H}_1 , so we can generate \mathbf{H}_2 in the same way. Besides, the static channel estimation during a given frame has been investigated in [11], and the time varying channel estimation as well as the mobile user tracking has been studied in [27]. Thus, we assume that the channel parameters can be well acquired in this paper.

IV. PROPOSED GRADIENT DESCENT BASED ALGORITHMS

With the given system model and the channel model, the achievable rate of the IRS-assisted THz MIMO system can be written as

$$R = \log_2 \left| \mathbf{I}_{N_s} + \frac{\rho}{\delta^2 N_s} (\mathbf{W}^H \mathbf{W})^{-1} \mathbf{W}^H (\mathbf{H}_2 \Phi \mathbf{H}_1) \mathbf{F} \mathbf{F}^H (\mathbf{H}_2 \Phi \mathbf{H}_1)^H \mathbf{W} \right|, \quad (11)$$

where $\mathbf{F} = \mathbf{F}_{\text{RF}} \mathbf{F}_{\text{BB}}$ and $\mathbf{W} = \mathbf{W}_{\text{RF}} \mathbf{W}_{\text{BB}}$. To convert the optimization problem (11) into a more evident form, the achievable rate maximization problem can be rewritten as

$$\begin{aligned} (\Phi^{\text{opt}}, \mathbf{W}^{\text{opt}}, \mathbf{F}^{\text{opt}}) &= \arg \max_{\Phi, \mathbf{W}, \mathbf{F}} R \\ \text{s.t. } \varphi_n &\in \mathcal{F}, \forall n = 1, \dots, N_{\text{IRS}}, \\ \Phi &= \text{diag}(\bar{\mu} e^{j\varphi_1}, \bar{\mu} e^{j\varphi_2}, \dots, \bar{\mu} e^{j\varphi_{N_{\text{IRS}}}}), \\ \|\mathbf{F}\|_F^2 &= N_s. \end{aligned} \quad (12)$$

From the non-convex and discrete optimization problem (12) we can note that there are some implicit properties. Firstly, the number of possible candidates of Φ is finite, since each entry $\{\varphi_n\}_{n=1}^{N_{\text{IRS}}}$ of Φ is discrete according to the hardware structure of the IRS. Secondly, \mathbf{F} and \mathbf{W} are unconstrained matrices. In addition, Φ is independent with \mathbf{F} and \mathbf{W} for the IRS assisted THz MIMO system.

Motivating by these distinguishing features, one available way of settling the above optimization problem is to first design \mathbf{F} and \mathbf{W} , and then optimize Φ . By utilizing the SVD operation, the channel \mathbf{H}_e can be decomposed into $\mathbf{H}_e = \mathbf{U} \mathbf{\Lambda} \mathbf{V}^H$, where \mathbf{U} is a $N_{\text{MS}} \times N_{\text{MS}}$ unitary matrix, $\mathbf{\Lambda}$ is a $N_{\text{MS}} \times N_{\text{BS}}$ dimensional matrix that contains a diagonal matrix and an all-zero matrix, and \mathbf{V} is a $N_{\text{BS}} \times N_{\text{BS}}$ unitary matrix, respectively. Furthermore, we decompose the unitary matrices

\mathbf{U} as $\mathbf{U} = [\mathbf{U}_1, \mathbf{U}_2]$ and \mathbf{V} as $\mathbf{V} = [\mathbf{V}_1, \mathbf{V}_2]$, where $\mathbf{U}_1 \in \mathbb{C}^{N_{\text{MS}} \times \text{rank}(\mathbf{H}_e)}$ is the sub-matrix of \mathbf{U} and $\mathbf{V}_1 \in \mathbb{C}^{N_{\text{BS}} \times \text{rank}(\mathbf{H}_e)}$ is the sub-matrix of \mathbf{V} . And then, \mathbf{H}_e can be written as

$$\begin{aligned} \mathbf{H}_e &= \mathbf{U} \mathbf{\Lambda} \mathbf{V}^H = [\mathbf{U}_1, \mathbf{U}_2] \begin{bmatrix} \mathbf{\Lambda}_1 & \mathbf{0} \\ \mathbf{0} & \mathbf{0} \end{bmatrix} [\mathbf{V}_1, \mathbf{V}_2]^H = [\mathbf{U}_1 \mathbf{\Lambda}_1, \mathbf{0}_{N_{\text{MS}} \times [N_{\text{BS}} - \text{rank}(\mathbf{H}_e)]}] \begin{bmatrix} \mathbf{V}_1^H \\ \mathbf{V}_2^H \end{bmatrix} \\ &= \mathbf{U}_1 \mathbf{\Lambda}_1 \mathbf{V}_1^H, \end{aligned} \quad (13)$$

where $\mathbf{\Lambda}_1 \in \mathbb{C}^{\text{rank}(\mathbf{H}_e) \times \text{rank}(\mathbf{H}_e)}$ is a diagonal matrix with the singular values arranged in a decreasing order. When $\mathbf{W} = \mathbf{U}_1$ and $\mathbf{F} = \mathbf{V}_1 \sqrt{N_s}$ which satisfies $\|\mathbf{F}\|_F^2 = N_s$, the data rate R in (11) can be rewritten as

$$\begin{aligned} R &= \log_2 \left| \mathbf{I}_{N_s} + \frac{\rho}{\delta^2 N_s} (\mathbf{W}^H \mathbf{W})^{-1} \mathbf{W}^H \mathbf{H}_e \mathbf{F} \mathbf{F}^H \mathbf{H}_e^H \mathbf{W} \right| \\ &= \log_2 \left| \mathbf{I}_{N_s} + \frac{\rho}{\delta^2} (\mathbf{U}_1^H \mathbf{U}_1)^{-1} \mathbf{U}_1^H \mathbf{H}_e \mathbf{V}_1 \mathbf{V}_1^H \mathbf{H}_e^H \mathbf{U}_1 \right| \\ &\stackrel{(a)}{=} \log_2 \left| \mathbf{I}_{N_s} + \frac{\rho}{\delta^2} \mathbf{U}_1^H \mathbf{H}_e \mathbf{V}_1 \mathbf{V}_1^H \mathbf{H}_e^H \mathbf{U}_1 \right|, \end{aligned} \quad (14)$$

where equation (a) is from $\mathbf{U}_1^H \mathbf{U}_1 = \mathbf{I}_{\text{rank}(\mathbf{H}_e) \times \text{rank}(\mathbf{H}_e)}$. Then, by using the SVD operation of $\mathbf{H}_e = \mathbf{U}_1 \mathbf{\Lambda}_1 \mathbf{V}_1^H$, (14) can be further formulated as

$$R = \log_2 \left| \mathbf{I}_{N_s} + \frac{\rho}{\delta^2} \mathbf{U}_1^H \mathbf{U}_1 \mathbf{\Lambda}_1 \mathbf{V}_1^H \mathbf{V}_1 \mathbf{V}_1^H (\mathbf{U}_1 \mathbf{\Lambda}_1 \mathbf{V}_1^H)^H \mathbf{U}_1 \right| \stackrel{(b)}{=} \log_2 \left| \mathbf{I}_{N_s} + \frac{\rho}{\delta^2} \mathbf{\Lambda}_1 \mathbf{\Lambda}_1^H \right|, \quad (15)$$

where equation (b) comes from $\mathbf{U}_1^H \mathbf{U}_1 = \mathbf{I}_{\text{rank}(\mathbf{H}_e) \times \text{rank}(\mathbf{H}_e)}$ and $\mathbf{V}_1^H \mathbf{V}_1 = \mathbf{I}_{\text{rank}(\mathbf{H}_e) \times \text{rank}(\mathbf{H}_e)}$.

From (15) we note that the matrix variable $\mathbf{\Lambda}_1$ is determined by Φ , and is not affected by \mathbf{F} or \mathbf{W} . Thus, we can maximize the data rate R by only optimizing Φ . Once the optimal Φ is obtained, the optimal precoder \mathbf{F} and combiner \mathbf{W} can be calculated by the SVD operation of $\mathbf{H}_e = \mathbf{U}_1 \mathbf{\Lambda}_1 \mathbf{V}_1^H$, where $\mathbf{\Lambda}_1 = \text{diag}[\sqrt{\eta_1}, \dots, \sqrt{\eta_{\text{rank}(\mathbf{H}_e)}}]^T$ and $\{\eta_i\}_{i=1}^{\text{rank}(\mathbf{H}_e)}$ can be treated as the virtual path gains of \mathbf{H}_e . After that, the CS-based solution can be adopted to decompose \mathbf{F} and \mathbf{W} into the RF part (e.g., $\mathbf{F}_{\text{RF}}, \mathbf{W}_{\text{RF}}$) and the baseband part (e.g., $\mathbf{F}_{\text{BB}}, \mathbf{W}_{\text{BB}}$), separately [28].

Hence, (15) can be further expressed as

$$\begin{aligned}
R &= \log_2 \left\| \mathbf{I}_{N_s} + \frac{\rho}{\delta^2} \begin{bmatrix} \eta_1 & 0 & \cdots & 0 \\ 0 & \eta_2 & \cdots & 0 \\ 0 & 0 & \ddots & 0 \\ 0 & 0 & \cdots & \eta_{\text{rank}(\mathbf{H}_e)} \end{bmatrix} \right\| \\
&= \log_2 \prod_{i=1}^{\text{rank}(\mathbf{H}_e)} \left(1 + \frac{\rho}{\delta^2} \eta_i \right) \\
&\stackrel{(c)}{<} \log_2 \prod_{i=1}^{\text{rank}(\mathbf{H}_e)} \left(e^{\rho \eta_i / \delta^2} \right) \\
&= \left(\sum_{i=1}^{\text{rank}(\mathbf{H}_e)} \eta_i \right) (\rho / \delta^2) \log_2 e,
\end{aligned} \tag{16}$$

where inequality (c) comes from Taylor expansion formulation and we note that $\{\eta_i\}_{i=1}^{\text{rank}(\mathbf{H}_e)}$ is usually small due to the serious path loss of THz waves.

Since solving the non-convex optimization problem (15) directly is very arduous, we can approximate this problem by optimizing the sum of the virtual path gains instead of designing the optimal phase shift matrix Φ . Hence, the phase optimization problem can be rewritten as

$$\Phi^{\text{opt}} = \arg \max_{\Phi} \sum_{i=1}^{\text{rank}(\mathbf{H}_e)} \eta_i \stackrel{(d)}{=} \arg \max_{\Phi} \text{Tr}(\mathbf{H}_e \mathbf{H}_e^H), \tag{17}$$

where equation (d) follows the result of linear algebra that satisfies $\text{Tr}(\mathbf{A}) = \sum_{i=1}^{N_s} \eta_i(\mathbf{A})$ for $\mathbf{A} \in \mathbb{C}^{N_s \times N_s}$. Through the above analysis, the simplified optimization problem (17) only involves one matrix variable Φ . Thus, the primary objective is to optimize $\text{Tr}(\mathbf{H}_e \mathbf{H}_e^H)$ in the following.

A. Conventional Gradient Descent Algorithm

To better cater to the gradient descent based methods, we need to convert the optimization problem (17) into a minimization problem as

$$\begin{aligned}
&\min_{\Phi} -\text{Tr}(\mathbf{H}_e \mathbf{H}_e^H) \\
&\text{s.t. } \varphi_n \in \mathbb{R}, \forall n = 1, \dots, N_{\text{IRS}}, \\
&\quad \Phi = \text{diag}(\bar{\mu} e^{j\varphi_1}, \bar{\mu} e^{j\varphi_2}, \dots, \bar{\mu} e^{j\varphi_{N_{\text{IRS}}}}),
\end{aligned} \tag{18}$$

where we temporarily consider the continuous phase shifts and we assume $\{\varphi_n\}_{n=1}^{N_{\text{IRS}}} \in \mathbb{R}$. After the optimal matrix Φ^{opt} is obtained, the continuous phase shifts can be mapped to the nearest values of discrete phase shifts. However, (18) is still a constrained optimization problem, because Φ possesses the diagonal feature and the constant-magnitude entries. Given this, we

define $\boldsymbol{\varphi} \triangleq \text{diag}(\varphi_1, \varphi_2, \dots, \varphi_{N_{\text{IRS}}})$, and then consider Φ as a function of $\boldsymbol{\varphi}$ where $\Phi(\boldsymbol{\varphi}) = \text{diag}(e^{j\varphi_1}, e^{j\varphi_2}, \dots, e^{j\varphi_{N_{\text{IRS}}}})$. With this definition, (18) can be reformulated as

$$\min_{\boldsymbol{\varphi}} -\text{Tr} \left\{ \mathbf{H}_2 \Phi(\boldsymbol{\varphi}) \mathbf{H}_1 [\mathbf{H}_2 \Phi(\boldsymbol{\varphi}) \mathbf{H}_1]^H \right\} = \min_{\boldsymbol{\varphi}} f(\boldsymbol{\varphi}), \quad (19)$$

where $f(\cdot)$ is a compound function relating to $\boldsymbol{\varphi}$, which can be further written as

$$\begin{aligned} f(\boldsymbol{\varphi}) &= -\text{Tr} \left\{ \mathbf{H}_2 \Phi(\boldsymbol{\varphi}) \mathbf{H}_1 [\mathbf{H}_2 \Phi(\boldsymbol{\varphi}) \mathbf{H}_1]^H \right\} \stackrel{(e)}{=} -\|\mathbf{H}_2 \Phi(\boldsymbol{\varphi}) \mathbf{H}_1\|_F^2 \\ &\stackrel{(f)}{=} -\|\text{vec}[\mathbf{H}_2 \Phi(\boldsymbol{\varphi}) \mathbf{H}_1]\|_F^2 = -\|(\mathbf{H}_1^T \otimes \mathbf{H}_2) \text{vec}[\Phi(\boldsymbol{\varphi})]\|_F^2 \\ &= -\text{vec}[\Phi(\boldsymbol{\varphi})]^H (\mathbf{H}_1^T \otimes \mathbf{H}_2)^H (\mathbf{H}_1^T \otimes \mathbf{H}_2) \text{vec}[\Phi(\boldsymbol{\varphi})], \end{aligned} \quad (20)$$

where equality (e) stems from the Frobenius norm operation and equality (f) is the vectorization operator. Note that in (20), $f(\boldsymbol{\varphi})$ is an unconstrained function since the matrix variable $\boldsymbol{\varphi}$ is not constrained. Thus, the C-GD algorithm is feasible to find a local optimal solution for the minimized optimization problem (19). In addition, the matrix product term $(\mathbf{H}_1^T \otimes \mathbf{H}_2)^H (\mathbf{H}_1^T \otimes \mathbf{H}_2)$ is independent of the variable matrix $\boldsymbol{\varphi}$. In order to further simplify (20), we define that

$$\mathbf{A} \triangleq -(\mathbf{H}_1^T \otimes \mathbf{H}_2)^H (\mathbf{H}_1^T \otimes \mathbf{H}_2), \quad (21)$$

$$\mathbf{x} \triangleq \text{vec}[\Phi(\boldsymbol{\varphi})], \quad (22)$$

where $\mathbf{A} \in \mathbb{C}^{N_{\text{BS}} N_{\text{MS}} \times N_{\text{IRS}}^2}$ is a conjugate symmetric positive definite matrix, and \mathbf{x} is a sparse vector with the dimension of $N_{\text{IRS}}^2 \times 1$. Then we can get that $f(\boldsymbol{\varphi})$ is equal to $\mathbf{x}^H \mathbf{A} \mathbf{x}$, and (21) can be rewritten as

$$\min_{\boldsymbol{\varphi}} f(\boldsymbol{\varphi}) = \min_{\boldsymbol{\varphi}} \mathbf{x}^H \mathbf{A} \mathbf{x}. \quad (23)$$

To calculate the gradient vector $\nabla_{\boldsymbol{\varphi}} f(\boldsymbol{\varphi})$ for the objective $f(\boldsymbol{\varphi})$, we expand $\mathbf{x}^H \mathbf{A} \mathbf{x}$ as

$$\begin{aligned} \mathbf{x}^H \mathbf{A} \mathbf{x} &= \left[e^{-j\varphi_1}, \mathbf{0}_{1 \times (N_{\text{IRS}}-1)}, e^{-j\varphi_2}, \mathbf{0}_{1 \times (N_{\text{IRS}}-1)}, \dots, e^{-j\varphi_{N_{\text{IRS}}}}, \mathbf{0}_{1 \times (N_{\text{IRS}}-1)} \right] \mathbf{A} \mathbf{x} \\ &= \left[\sum_{p=1}^{N_{\text{IRS}}} e^{-j\varphi_p} \mathbf{A}_{(p-1)N_{\text{IRS}}+p,1}, \dots, \sum_{p=1}^{N_{\text{IRS}}} e^{-j\varphi_p} \mathbf{A}_{(p-1)N_{\text{IRS}}+p,N_{\text{IRS}}} \right] \mathbf{x} \\ &= \sum_{q=1}^{N_{\text{IRS}}} e^{j\varphi_q} \left[\sum_{p=1}^{N_{\text{IRS}}} e^{-j\varphi_p} \mathbf{A}_{(p-1)N_{\text{IRS}}+p,(q-1)N_{\text{IRS}}+q} \right] \\ &= \sum_{p=1}^{N_{\text{IRS}}} \sum_{q=1}^{N_{\text{IRS}}} e^{j(\varphi_q - \varphi_p)} \mathbf{A}_{(p-1)N_{\text{IRS}}+p,(q-1)N_{\text{IRS}}+q}, \end{aligned} \quad (24)$$

where $\mathbf{0}_{1 \times (N_{\text{IRS}}-1)}$ is the all zero vector with the dimension of $1 \times (N_{\text{IRS}} - 1)$ and the matrix $\mathbf{A}_{(p-1)N_{\text{IRS}}+p,(q-1)N_{\text{IRS}}+q}$ denotes the $\{(p-1)N_{\text{IRS}} + p, (q-1)N_{\text{IRS}} + q\}$ th entry of matrix

A. Since $\mathbf{A}^H = \mathbf{A}$, each diagonal entry of \mathbf{A} is a real value and $\mathbf{A}_{i,j} + \mathbf{A}_{j,i} = 2\mathcal{R}\{\mathbf{A}_{i,j}\}$, $\forall i, j = 1, \dots, N_{\text{IRS}}, i \neq j$. Therefore, (24) can be further simplified as

$$\mathbf{x}^H \mathbf{A} \mathbf{x} = \sum_{p=1}^{N_{\text{IRS}}} \mathbf{A}_{(p-1)N_{\text{IRS}}+p, (p-1)N_{\text{IRS}}+p} + 2\mathcal{R} \left\{ \sum_{p=1}^{N_{\text{IRS}}} \sum_{q>p}^{N_{\text{IRS}}} e^{j(\varphi_q - \varphi_p)} \mathbf{A}_{(p-1)N_{\text{IRS}}+p, (q-1)N_{\text{IRS}}+q} \right\}, \quad (25)$$

Given this, the n th element of the gradient vector $\nabla_{\varphi} f(\varphi)$ is calculated as

$$\begin{aligned} \frac{\partial f(\varphi)}{\partial \varphi_n} &= \frac{\partial(\mathbf{x}^H \mathbf{A} \mathbf{x})}{\partial \varphi_n} \\ &= 2\mathcal{R} \left\{ -j e^{-j\varphi_n} \sum_{q>n}^{N_{\text{IRS}}} e^{j\varphi_q} \mathbf{A}_{(n-1)N_{\text{IRS}}+n, (q-1)N_{\text{IRS}}+q} + j e^{j\varphi_n} \sum_{n>p}^{N_{\text{IRS}}} e^{-j\varphi_p} \mathbf{A}_{(p-1)N_{\text{IRS}}+p, (n-1)N_{\text{IRS}}+n} \right\}, \end{aligned} \quad (26)$$

After computing all the $\partial f(\varphi)/\partial \varphi_n, \forall n = 1, 2, \dots, N_{\text{IRS}}$, $\nabla_{\varphi} f(\varphi)$ can be expressed as

$$\nabla_{\varphi} f(\varphi) = \left[\frac{\partial f(\varphi)}{\partial \varphi_1}, \frac{\partial f(\varphi)}{\partial \varphi_2}, \dots, \frac{\partial f(\varphi)}{\partial \varphi_{N_{\text{IRS}}}} \right]^T, \quad (27)$$

Following the gradient direction $\nabla_{\varphi} f(\varphi)$, the value of the objective function $f(\varphi)$ is able to descend by replacing φ with $\varphi - \lambda \text{diag}(\nabla_{\varphi} f(\varphi))$, where λ is the iterative step size. During the i th iteration, the updated $\varphi^{(i+1)}$ and the renewed $f(\varphi^{i+1})$ can be respectively written as

$$\varphi^{i+1} = \varphi^i - \lambda \text{diag}(\nabla_{\varphi} f(\varphi^i)), \quad (28)$$

$$f(\varphi^{i+1}) = f\{\varphi^i - \lambda \text{diag}(\nabla_{\varphi} f(\varphi^i))\}. \quad (29)$$

The proposed C-GD algorithm continues to execute (28) and (29) until the maximum number of iterations is reached. Then, $f(\varphi)$ converges to a minimum value and φ get a locally optimal point φ^{opt} . After that, each entry of φ^{opt} is mapped into the nearest discrete phase shifts from \mathcal{F} , the optimal phase shift matrix Φ^{opt} can be given as $\Phi^{\text{opt}} = \exp(\varphi^{\text{opt}})$. Finally, Λ_1 can be realized by $\mathbf{H}_2 \Phi^{\text{opt}} \mathbf{H}_1 = \mathbf{U}_1 \Lambda_1 \mathbf{V}_1^H$, and the optimized R can be computed based on (15) for the IRS-enabled THz MIMO system.

B. Adaptive Gradient Descent Algorithm

The C-GD algorithm obtains the fixed step size λ by the simulation experiment, which suffers from high complexity and low efficiency. Stated thus, a novel A-GD algorithm is developed to determine a suitable step size λ^i by dynamically updating the step size during i th iterative process.

In order to configure an appropriate step size λ^i during the iterative process, (28) can be expanded as

$$\begin{aligned} f(\boldsymbol{\varphi}^{i+1}) &= [\mathbf{x}^{(i+1)}]^H \mathbf{A} \mathbf{x}^{(i+1)} \\ &= \sum_{q=1}^{N_{\text{IRS}}} e^{j(\varphi_q^i + \Delta\varphi_q^i)} \sum_{p=1}^{N_{\text{IRS}}} \left[e^{-j(\varphi_p^i + \Delta\varphi_p^i)} \mathbf{A}_{(p-1)N_{\text{IRS}}+p, (q-1)N_{\text{IRS}}+q} \right] \\ &= \sum_{p=1}^{N_{\text{IRS}}} \sum_{q=1}^{N_{\text{IRS}}} \left[e^{j(\varphi_q^i + \Delta\varphi_q^i) - j(\varphi_p^i + \Delta\varphi_p^i)} \mathbf{A}_{(p-1)N_{\text{IRS}}+p, (q-1)N_{\text{IRS}}+q} \right], \end{aligned} \quad (30)$$

where $\Delta\varphi_n^i = -\lambda^i \partial f(\boldsymbol{\varphi}^i) / \partial \varphi_n^i$ for $n = 1, 2, \dots, N_{\text{IRS}}$. By using $\mathbf{A} = \mathbf{A}^H$, $f(\boldsymbol{\varphi}^{i+1})$ can be further simplified as

$$\begin{aligned} f(\boldsymbol{\varphi}^{i+1}) &= \sum_{p=1}^{N_{\text{IRS}}} \mathbf{A}_{(p-1)N_{\text{IRS}}+p, (p-1)N_{\text{IRS}}+p} \\ &\quad + 2\mathcal{R} \left\{ \sum_{p=1}^{N_{\text{IRS}}} \sum_{q>p}^{N_{\text{IRS}}} \left\{ e^{j(\varphi_q^i - \varphi_p^i)} e^{j\lambda^i \left[\frac{\partial f(\boldsymbol{\varphi}^i)}{\partial \varphi_p^i} - \frac{\partial f(\boldsymbol{\varphi}^i)}{\partial \varphi_q^i} \right]} \mathbf{A}_{(p-1)N_{\text{IRS}}+p, (q-1)N_{\text{IRS}}+q} \right\} \right\}, \end{aligned} \quad (31)$$

According to (31), the partial derivative terms $\partial f(\boldsymbol{\varphi}^i) / \partial \varphi_p^i$ and $\partial f(\boldsymbol{\varphi}^i) / \partial \varphi_q^i$ of the gradient vector $\nabla_{\boldsymbol{\varphi}} f(\boldsymbol{\varphi}^i)$ are obtained during the i th iteration process. For the $(i+1)$ th iteration, $f(\boldsymbol{\varphi}^{i+1})$ is only determined by the step size λ^i . To minimize the value of $f(\boldsymbol{\varphi}^{i+1})$, we are to seek a much better λ^i and the optimization problem can be expressed as

$$\begin{aligned} \lambda^i &= \arg \min_{\lambda^i} f(\boldsymbol{\varphi}^{i+1}) \\ &= \arg \min_{\lambda^i} \mathcal{R} \left\{ \sum_{p=1}^{N_{\text{IRS}}} \sum_{q>p}^{N_{\text{IRS}}} e^{j(\varphi_q^i - \varphi_p^i)} e^{j\lambda^i \left[\frac{\partial f(\boldsymbol{\varphi}^i)}{\partial \varphi_p^i} - \frac{\partial f(\boldsymbol{\varphi}^i)}{\partial \varphi_q^i} \right]} \mathbf{A}_{(p-1)N_{\text{IRS}}+p, (q-1)N_{\text{IRS}}+q} \right\}, \end{aligned} \quad (32)$$

In order to optimize (32), the A-GD algorithm replaces $e^{j\lambda^i [\partial f(\boldsymbol{\varphi}^i) / \partial \varphi_p^i - \partial f(\boldsymbol{\varphi}^i) / \partial \varphi_q^i]}$ with the second-order Taylor expansion formulation. Thus, (32) can be approximated as

$$\begin{aligned} \lambda^i &\approx \arg \min_{\lambda^i} \mathcal{R} \left\{ \sum_{p=1}^{N_{\text{IRS}}} \sum_{q>p}^{N_{\text{IRS}}} e^{j(\varphi_q^i - \varphi_p^i)} \mathbf{A}_{(p-1)N_{\text{IRS}}+p, (q-1)N_{\text{IRS}}+q} \right. \\ &\quad \left. \times \left[1 + j\lambda^i \left[\frac{\partial f(\boldsymbol{\varphi}^i)}{\partial \varphi_p^i} - \frac{\partial f(\boldsymbol{\varphi}^i)}{\partial \varphi_q^i} \right] + \frac{(j\lambda^i)^2}{2} \left[\frac{\partial f(\boldsymbol{\varphi}^i)}{\partial \varphi_p^i} - \frac{\partial f(\boldsymbol{\varphi}^i)}{\partial \varphi_q^i} \right]^2 \right] \right\} \\ &= \arg \min_{\lambda^i} C_0 + C_1 \lambda^i + C_2 (\lambda^i)^2, \end{aligned} \quad (33)$$

where (33) is a quadratic function with the variable λ^i .

It is worth noting that there are two different cases for the quadratic function in (33), including the positive value of term C_2 and the negative value of term C_2 . For these two cases of term

Algorithm 1 Proposed A-GD Algorithm

Require: $\mathbf{H}_1, \mathbf{H}_2, \rho, N_s, \delta^2, \mathcal{F}, I, i = 0,$

1: Initialize $\mathbf{A} = -(\mathbf{H}_1^T \otimes \mathbf{H}_2)^H (\mathbf{H}_1^T \otimes \mathbf{H}_2), f_{\max} = 0,$

$\boldsymbol{\varphi}^0 = \mathbf{0}_{N_{\text{IRS}} \times 1}, \mathbf{x}^0 = \text{vec} [\Phi(\boldsymbol{\varphi}^0)],$

2: **while** $i \leq I$ **do**

3: Calculate the gradient vector $\nabla_{\boldsymbol{\varphi}} f(\boldsymbol{\varphi}^i)$ in (27),

4: Compute the step size λ^i in (34),

5: Update $\boldsymbol{\varphi}^{i+1} = \boldsymbol{\varphi}^i - \lambda^i \text{diag}(\nabla_{\boldsymbol{\varphi}} f(\boldsymbol{\varphi}^i)),$

$\mathbf{x}^{i+1} = \text{vec} [\Phi(\boldsymbol{\varphi}^i)],$

6: Renew $f(\boldsymbol{\varphi}^{i+1}) = f\{\boldsymbol{\varphi}^i - \lambda^i \text{diag}(\nabla_{\boldsymbol{\varphi}} f(\boldsymbol{\varphi}^i))\},$

7: **if** $f(\boldsymbol{\varphi}^{i+1}) > f_{\max}$ **do**

8: $f_{\max} = f(\boldsymbol{\varphi}^{i+1}), \boldsymbol{\varphi}^{\text{opt}} = \boldsymbol{\varphi}^{i+1},$

9: **end if**

10: $i = i + 1,$

11: **end while**

12: Map each diagonal entry of $\boldsymbol{\varphi}^{\text{opt}}$ into discrete phase shifts from $\mathcal{F},$

13: Calculate $\Phi^{\text{opt}} = \exp(\boldsymbol{\varphi}^{\text{opt}})$ and R by (11).

Ensure: Φ^{opt}, R

C_2 , the step size λ^i is calculated in a different way. Specifically, the adaptive step size of each case for the A-GD algorithm can be written as

$$\lambda^i = \begin{cases} -C_1/(2C_2), & C_2 > 0 \\ |C_1|/|C_2|, & C_2 < 0. \end{cases} \quad (34)$$

The detailed steps of the A-GD algorithm for solving (11) is illustrated in **Algorithm 1**.

V. PROPOSED ALTERNATING OPTIMIZATION ALGORITHM

Though the C-GD algorithm and A-GD algorithm are able to settle the non-convex optimization problem, both of them inherit heavy calculation load in terms of computing the gradient descent vector and initializing the matrix \mathbf{A} . In this section, a novel AO algorithm is proposed to mitigate the data rate maximization problem involving the multiple matrix variables $(\mathbf{F}_{\text{BB}}, \mathbf{F}_{\text{RF}}, \mathbf{W}_{\text{BB}}, \mathbf{W}_{\text{RF}}, \Phi)$. Concretely, the AO algorithm contains a CBC algorithm to seek the precoders (or combiners) and a linear search algorithm to obtain the phase shift matrix.

A. CBC Algorithm

To start with, we first propose the CBC algorithm to design \mathbf{F}_{RF} , \mathbf{F}_{BB} , \mathbf{W}_{RF} and \mathbf{W}_{BB} with a given Φ . However, the multiple matrix variable optimization to maximize the data rate R is intractable. As a common practice, the joint precoder and combiner design is usually transformed into two separate subproblems, i.e., one precoding problem about $(\mathbf{F}_{\text{BB}}, \mathbf{F}_{\text{RF}})$, and one combining problem about $(\mathbf{W}_{\text{BB}}, \mathbf{W}_{\text{RF}})$ [17]. Thus, the precoding problem can be formulated as

$$\begin{aligned} (\mathbf{F}_{\text{BB}}^{\text{opt}}, \mathbf{F}_{\text{RF}}^{\text{opt}}) &= \arg \min_{\mathbf{F}_{\text{BB}}, \mathbf{F}_{\text{RF}}} \|\mathbf{F}_{\text{opt}} - \mathbf{F}_{\text{RF}} \mathbf{F}_{\text{BB}}\|_F^2 \\ \text{s.t. } \mathbf{F}_{\text{RF}} &\in \mathcal{F}_{\text{RF}}, \|\mathbf{F}_{\text{RF}} \mathbf{F}_{\text{BB}}\|_F^2 = N_s, \end{aligned} \quad (35)$$

where $\mathbf{F}_{\text{opt}} \in \mathcal{C}^{N_{\text{BS}} \times N_s}$ is the optimal fully-digital precoding matrix and equals to $\mathbf{V}_{N_s} \mathbf{\Gamma}$, where $\mathbf{\Gamma} \in \mathcal{C}^{N_s \times N_s}$ denotes the water-filling power allocation matrix and $\mathbf{V}_{N_s} \in \mathcal{C}^{N_{\text{BS}} \times N_s}$ is the first N_s columns of \mathbf{V} that comes from the SVD operation of $\mathbf{H}_e = \mathbf{U} \mathbf{\Sigma} \mathbf{V}^H$. Similar to the precoding problem (35), the combining problem can be also formulated as

$$\begin{aligned} (\mathbf{W}_{\text{BB}}^{\text{opt}}, \mathbf{W}_{\text{RF}}^{\text{opt}}) &= \arg \min_{\mathbf{W}_{\text{BB}}, \mathbf{W}_{\text{RF}}} \|\mathbf{W}_{\text{opt}} - \mathbf{W}_{\text{RF}} \mathbf{W}_{\text{BB}}\|_F^2 \\ \text{s.t. } \mathbf{W}_{\text{RF}} &\in \mathcal{W}_{\text{RF}}, \end{aligned} \quad (36)$$

where $\mathbf{W}_{\text{opt}} \in \mathcal{C}^{N_{\text{MS}} \times N_s}$ is the optimal fully-digital combining matrix and equals to the first N_s columns of \mathbf{U} , which can be denoted as \mathbf{U}_{N_s} .

Consequently, the joint of \mathbf{F}_{RF} , \mathbf{F}_{BB} , \mathbf{W}_{RF} , and \mathbf{W}_{BB} is decomposed into two subproblems (35) and (36). Next, the CBC algorithm is presented to solve the precoding problem and combining problem. Since these two problems share the similar form except that the precoding problem has an additional constraint $\|\mathbf{F}_{\text{RF}} \mathbf{F}_{\text{BB}}\|_F^2 = N_s$, we take the solution of the precoding problem as an example.

The objective of (35) is to make $\mathbf{F}_{\text{RF}} \mathbf{F}_{\text{BB}}$ approach \mathbf{F}_{opt} . However, the main obstacle existing in (35) is that each element in \mathbf{F}_{RF} has a constant-magnitude constraint. We denote the l th column of \mathbf{F}_{opt} as $\mathbf{f}_{\text{opt}}^{(l)}$. Interestingly, one property of the vector $\mathbf{f}_{\text{opt}}^{(l)}$ under the constant-magnitude constraint is that, an arbitrary vector without constant-magnitude constraint can be expressed as the linear combination of two vectors under the constant-magnitude constraint [29]. Thus, the l th column of \mathbf{F}_{opt} can be expressed as

$$\mathbf{f}_{\text{opt}}^{(l)} = a_l \mathbf{p}_l + b_l \mathbf{q}_l, \quad (37)$$

where \mathbf{p}_l and \mathbf{q}_l are two vectors under the constant-magnitude constraint. a_l and b_l are two linear combination factors. One solution of (37) is that $a_l = b_l = d_{\text{max}}$, where d_{max} is the

largest magnitude of the elements in $\mathbf{f}_{\text{opt}}^{(l)}$, and then calculate \mathbf{p}_l and \mathbf{q}_l . With such a feature of the constant-magnitude vector, we can set the $(2l - 1)$ th column and the $(2l)$ th column of \mathbf{F}_{RF} as $\mathbf{f}_{\text{RF}}^{(2l-1)} = \mathbf{p}_l$ and $\mathbf{f}_{\text{RF}}^{(2l)} = \mathbf{q}_l$. Meanwhile, the $(2l - 1)$ th and $(2l)$ th elements of $\mathbf{f}_{\text{BB}}^{(l)}$ are set as $d_{2l-1} = a_l$ and $d_{2l} = b_l$. As a result, we have

$$\mathbf{f}_{\text{opt}}^{(l)} = \mathbf{F}_{\text{RF}} \mathbf{f}_{\text{BB}}^{(l)} = \left[\dots, \mathbf{f}_{\text{RF}}^{(2l-1)}, \mathbf{f}_{\text{RF}}^{(2l)}, \dots \right] [0, \dots, 0, d_{2l-1}, d_{2l}, 0, \dots, 0]^T, \quad (38)$$

Following (38), each $\mathbf{f}_{\text{opt}}^{(l)}$ can be expressed as the linear combination of two column vectors in \mathbf{F}_{RF} . Recall that the dimensions of \mathbf{F}_{opt} and \mathbf{F}_{RF} are $N_{\text{BS}} \times N_s$ and $N_{\text{BS}} \times M_{\text{BS}}$. To transmit N_s data streams, the number of RF chains M_{BS} is no smaller than N_s . Thus, we divide the minimization of $\|\mathbf{F}_{\text{opt}} - \mathbf{F}_{\text{RF}} \mathbf{F}_{\text{BB}}\|_F^2$ into two cases according to the relation between M_{BS} and $2N_s$ as follows.

Case 1 ($M_{\text{BS}} \geq 2N_s$): All $\mathbf{f}_{\text{opt}}^{(l)}$ can be expressed as (38), and then \mathbf{F}_{opt} can be represented as

$$\mathbf{F}_{\text{opt}} = \mathbf{QD} = \begin{bmatrix} \mathbf{p}_1, \mathbf{q}_1, \dots, \mathbf{p}_{N_s}, \mathbf{q}_{N_s} \end{bmatrix} \begin{bmatrix} \mathbf{d}_1 \\ \vdots \\ \mathbf{d}_{N_s} \end{bmatrix}, \quad (39)$$

where $\mathbf{d}_l = [a_l, b_l]^T$. Since $M_{\text{BS}} \geq 2N_s$, we can make the first $2N_s$ columns of \mathbf{F}_{RF} as \mathbf{Q} and the first $2N_s$ rows of \mathbf{F}_{BB} as \mathbf{D} . Meanwhile, the remaining $(M_{\text{BS}} - 2N_s)$ rows of \mathbf{F}_{BB} can be set zero, and the remaining $(M_{\text{BS}} - 2N_s)$ columns of \mathbf{F}_{RF} can be set arbitrarily. Thus, \mathbf{F}_{opt} can be exactly expressed as $\mathbf{F}_{\text{RF}} \mathbf{F}_{\text{BB}}$, which is the optimal solution of problem (35).

Case 2 ($N_s \leq M_{\text{BS}} < 2N_s$): Since $M_{\text{BS}} < 2N_s$, the columns of \mathbf{F}_{RF} and the rows of \mathbf{F}_{BB} are insufficient to be set as \mathbf{Q} and \mathbf{D} . Fortunately, according to [30], we note that $\|\mathbf{f}_{\text{opt}}^{(l)}\|_\infty \leq \sqrt{L_p/N_{\text{BS}}}$, where L_p is the number of multipath of the THz channel. This property implies that the amplitude differences of the elements in $\mathbf{f}_{\text{opt}}^{(l)}$ are smaller than $\sqrt{L_p/N_{\text{BS}}}$. Due to the sparse nature of the THz channel, L_p is usually small [7]. Considering the deployment of ultra-massive antennas at THz band, e.g., $N_{\text{BS}} = 512$ antennas, $\sqrt{L_p/N_{\text{BS}}}$ is far less than 1. As a result, the amplitude of each element in $\|\mathbf{f}_{\text{opt}}^{(l)}\|_1/N_{\text{BS}}$, which guarantees that $\mathbf{f}_{\text{opt}}^{(l)}$ can be approximated as

$$\mathbf{f}_{\text{opt}}^{(l)} \approx \mathbf{F}_{\text{RF}} \mathbf{f}_{\text{BB}}^{(l)} = [\dots, \mathbf{f}_{\text{RF}}^{(l)}, \dots] [0, \dots, 0, d_l, 0, \dots, 0]^T, \quad (40)$$

where d_l is the l th element of $\mathbf{f}_{\text{BB}}^{(l)}$. In addition, the optimal d_l and $\mathbf{f}_{\text{RF}}^{(l)}$ for $\mathbf{f}_{\text{opt}}^{(l)}$ are known as

$$d_l = \frac{\|\mathbf{f}_{\text{opt}}^{(l)}\|_1}{N_{\text{BS}}}, \quad (41)$$

$$\mathbf{f}_{\text{RF}}^{(l)} = [e^{j^* \frac{f_1}{|f_1|}}, \dots, e^{j^* \frac{f_q}{|f_q|}}, \dots, e^{j^* \frac{f_{N_{\text{BS}}}}{|f_{N_{\text{BS}}}|}}]^T, \quad (42)$$

where f_q is the q th element of $\mathbf{f}_{\text{opt}}^{(l)}$. The phase information of $\mathbf{f}_{\text{opt}}^{(l)}$ is contained in $\mathbf{f}_{\text{RF}}^{(l)}$, while the approximation error comes from the amplitude differences between the element in $\mathbf{f}_{\text{opt}}^{(l)}$ and $\|\mathbf{f}_{\text{opt}}^{(l)}\|_1/N_{\text{BS}}$, which is small as we have analyzed before.

Currently, there are two approaches expressing the vector $\mathbf{f}_{\text{opt}}^{(l)}$. One is utilizing two columns in \mathbf{F}_{RF} to exactly express $\mathbf{f}_{\text{opt}}^{(l)}$ as shown in (38), and the other is employing one column in \mathbf{F}_{RF} to approximate $\mathbf{f}_{\text{opt}}^{(l)}$ as shown in (40). Since the first method owns the advantage of performance lossless, we aim to express the columns of $\mathbf{f}_{\text{opt}}^{(l)}$ by (38) as more as possible. Under the case of $M_{\text{BS}} < 2N_s$, we at most select $(M_{\text{BS}} - N_s)$ columns of $\mathbf{f}_{\text{opt}}^{(l)}$ that are expressed by (38), while the remaining $(2N_s - M_{\text{BS}})$ columns need to be approximated by (40). One further question is how to classify these $(M_{\text{BS}} - N_s)$ columns and $(2N_s - M_{\text{BS}})$ columns. Noting that the performance penalty is only caused by the approximation error in (40), we adopt the variance σ_l^2 to quantify the amplitude difference of each element in $\mathbf{f}_{\text{opt}}^{(l)}$, and the σ_l^2 can be defined as

$$\sigma_l^2 \triangleq \sum_{q=1}^{N_{\text{BS}}} \left(f_q - \frac{\|\mathbf{f}_{\text{opt}}^{(l)}\|_1}{N_{\text{BS}}} \right)^2, \quad (43)$$

where f_q is the amplitude of the q th element in $\mathbf{f}_{\text{opt}}^{(l)}$. Based on the classification criteria, we select $(2N_s - M_{\text{BS}})$ columns with the least variance σ_l^2 from $\mathbf{f}_{\text{opt}}^{(l)}$ to be approximated as (40), and then the remaining $(M_{\text{BS}} - N_s)$ columns are calculated as (38). The important steps of the CBC algorithm for the precoding problem (35) are presented in **Algorithm 2**. Similarly, the combining problem (36) can also be handled by the CBC algorithm without the normalization step $\mathbf{F}_{\text{BB}} \leftarrow \frac{\sqrt{N_s}}{\|\mathbf{F}_{\text{RF}}\mathbf{F}_{\text{BB}}\|_F} \mathbf{F}_{\text{BB}}$.

B. Linear Search Algorithm

With the given precoders and combiners solved by CBC algorithm, the linear search algorithm aims to optimize N_{IRS} reflection coefficient variables $\{\phi_n = \bar{\mu}e^{j\varphi_n}\}_{n=1}^{N_{\text{IRS}}}$ by following the one-the-rest criterion. Concretely, this criterion indicates that only one phase shift variable can be selected from a finite phase shift set \mathcal{F} while the rest $(N_{\text{IRS}} - 1)$ phase shift variables remain fixed. Remarkably, our proposed linear search algorithm endures the linear complexity growth with the increasing number of IRS elements.

Algorithm 2 CBC Algorithm

Require: \mathbf{F}_{opt}

- 1: **Case 1:** Compute \mathbf{F}_{RF} and \mathbf{F}_{BB} as (39);
- 2: **Case 2:**
- 3: Compute σ_l^2 of $\mathbf{f}_{\text{opt}}^{(l)}$,
- 4: Use the *classification criteria* (43),
- 5: **for** $l = 1 : N_s$
- 6: Calculate $\mathbf{f}_{\text{RF}}^{(l)}$ and $\mathbf{f}_{\text{BB}}^{(l)}$ as (38) or (40),
- 7: **end for**
- 8: Normalize \mathbf{F}_{BB} as $\mathbf{F}_{\text{BB}} \leftarrow \frac{\sqrt{N_s}}{\|\mathbf{F}_{\text{RF}}\mathbf{F}_{\text{BB}}\|_F} \mathbf{F}_{\text{BB}}$.

Ensure: \mathbf{F}_{RF} and \mathbf{F}_{BB}

According to (12), the data rate of the IRS-enabled THz MIMO system can be formulated as

$$\begin{aligned}
 R &= \log_2 \left| \mathbf{I}_{N_s} + \frac{\rho}{\delta^2 N_s} (\mathbf{W}^H \mathbf{W})^{-1} \mathbf{W}^H (\mathbf{H}_2 \Phi \mathbf{H}_1) \mathbf{F} \mathbf{F}^H (\mathbf{H}_2 \Phi \mathbf{H}_1)^H \mathbf{W} \right| \\
 &\stackrel{(g)}{\geq} \log_2 \left(|\mathbf{I}_{N_s}| + \left| \frac{\rho}{\delta^2 N_s} (\mathbf{W}^H \mathbf{W})^{-1} (\mathbf{W}^H \mathbf{H}_2 \Phi \mathbf{H}_1 \mathbf{F}) (\mathbf{W}^H \mathbf{H}_2 \Phi \mathbf{H}_1 \mathbf{F})^H \right| \right) \\
 &\stackrel{(h)}{=} \log_2 \left(|\mathbf{I}_{N_s}| + \left| (\mathbf{W}^H \mathbf{W})^{-1} \left| \frac{\rho}{\delta^2 N_s} (\mathbf{W}^H \mathbf{H}_2 \Phi \mathbf{H}_1 \mathbf{F}) (\mathbf{W}^H \mathbf{H}_2 \Phi \mathbf{H}_1 \mathbf{F})^H \right| \right| \right),
 \end{aligned} \tag{44}$$

where definition (g) satisfies $|\mathbf{A} + \mathbf{B}| \geq |\mathbf{A}| + |\mathbf{B}|$ for any positive semidefinite matrices \mathbf{A} and \mathbf{B} , definition (h) holds $|\mathbf{A}\mathbf{B}| = |\mathbf{A}| |\mathbf{B}|$ for any square matrices \mathbf{A} and \mathbf{B} . Since both precoding matrix \mathbf{F} and combining matrix \mathbf{W} are constant matrices, the achievable rate maximization problem is further simplified as

$$\begin{aligned}
 \Phi^{\text{opt}} &= \arg \max_{\Phi} \tilde{R} \\
 \text{s.t. } \varphi_n &\in \mathcal{F}, \forall n = 1, \dots, N_{\text{IRS}} \\
 \Phi &= (\bar{\mu} e^{j\varphi_1}, \bar{\mu} e^{j\varphi_2}, \dots, \bar{\mu} e^{j\varphi_{N_{\text{IRS}}}}),
 \end{aligned} \tag{45}$$

where we define \tilde{R} as

$$\tilde{R} = \log_2 \left| \frac{\rho}{\delta^2 N_s} (\mathbf{W}^H \mathbf{H}_2 \Phi \mathbf{H}_1 \mathbf{F}) (\mathbf{W}^H \mathbf{H}_2 \Phi \mathbf{H}_1 \mathbf{F})^H \right|, \tag{46}$$

Here we can define $\bar{\mathbf{H}}_1 = \mathbf{H}_1 \mathbf{F} = [\bar{\mathbf{h}}_{1,1}, \dots, \bar{\mathbf{h}}_{1,N_{\text{IRS}}}]^H$ and $\bar{\mathbf{H}}_2 = \mathbf{W}^H \mathbf{H}_2 = [\bar{\mathbf{h}}_{2,1}, \dots, \bar{\mathbf{h}}_{2,N_{\text{IRS}}}]$, where $\bar{\mathbf{h}}_{1,n} \in \mathbb{C}^{N_s \times 1}$ and $\bar{\mathbf{h}}_{2,n} \in \mathbb{C}^{N_s \times 1}$. With the defined form, $\bar{\mathbf{H}}_e$ can be expressed as

$$\bar{\mathbf{H}}_e = (\bar{\mathbf{H}}_2 \Phi \bar{\mathbf{H}}_1) = \sum_{n=1}^{N_{\text{IRS}}} \phi_n \bar{\mathbf{h}}_{2,n} \bar{\mathbf{h}}_{1,n}^H, \tag{47}$$

By resorting to (47), we are able to rewrite (46) as

$$\begin{aligned}
\tilde{R} &= \log_2 \left| \frac{\rho}{\delta^2 N_s} (\bar{\mathbf{H}}_2 \Phi \bar{\mathbf{H}}_1) (\bar{\mathbf{H}}_2 \Phi \bar{\mathbf{H}}_1)^H \right| \\
&= \log_2 \left| \frac{\rho}{\delta^2 N_s} \left(\sum_{n=1}^{N_{\text{IRS}}} \phi_n \bar{\mathbf{h}}_{2,n} \bar{\mathbf{h}}_{1,n}^H \right) \left(\sum_{n=1}^{N_{\text{IRS}}} \phi_n \bar{\mathbf{h}}_{2,n} \bar{\mathbf{h}}_{1,n}^H \right)^H \right| \\
&= \log_2 \left| \frac{\rho}{\delta^2 N_s} \left(\sum_{n=1}^{N_{\text{IRS}}} \phi_n \bar{\mathbf{h}}_{2,n} \bar{\mathbf{h}}_{1,n}^H \right) \left(\sum_{n=1}^{N_{\text{IRS}}} \phi_n^* \bar{\mathbf{h}}_{1,n} \bar{\mathbf{h}}_{2,n}^H \right) \right|,
\end{aligned} \tag{48}$$

To solve the optimization problem with N_{IRS} reflection coefficient variables, the linear search algorithm is investigated under the criterion of one-the-rest, which guarantees to optimize only one variable at a time. Concretely, when we optimize ϕ_n , the rest variables $\{\phi_i\}_{i=1, i \neq n}^{N_{\text{IRS}}}$ are treated as constants during the optimization process. On the basic of this criterion, the objective function in terms of only one variable ϕ_n can be rewritten as

$$\begin{aligned}
\tilde{R}(\phi_n) &= \log_2 \left| \frac{\rho}{\delta^2 N_s} \left(\phi_n \bar{\mathbf{h}}_{2,n} \bar{\mathbf{h}}_{1,n}^H + \sum_{i=1, i \neq n}^{N_{\text{IRS}}} \phi_i \bar{\mathbf{h}}_{2,i} \bar{\mathbf{h}}_{1,i}^H \right) \left(\phi_n^* \bar{\mathbf{h}}_{1,n} \bar{\mathbf{h}}_{2,n}^H + \sum_{j=1, j \neq n}^{N_{\text{IRS}}} \phi_j^* \bar{\mathbf{h}}_{1,j} \bar{\mathbf{h}}_{2,j}^H \right) \right| \\
&= \log_2 \left| \frac{\rho}{\delta^2 N_s} (\mathbf{P}_n + \phi_n \mathbf{Q}_n + \phi_n^* \mathbf{Q}_n^H) \right|,
\end{aligned} \tag{49}$$

where

$$\begin{aligned}
\mathbf{P}_n &= \bar{\mu}^2 \bar{\mathbf{h}}_{2,n} \bar{\mathbf{h}}_{1,n}^H \bar{\mathbf{h}}_{1,n} \bar{\mathbf{h}}_{2,n}^H + \left(\sum_{i=1, i \neq n}^{N_{\text{IRS}}} \phi_i \bar{\mathbf{h}}_{2,i} \bar{\mathbf{h}}_{1,i}^H \right) \left(\sum_{j=1, j \neq n}^{N_{\text{IRS}}} \phi_j^* \bar{\mathbf{h}}_{1,j} \bar{\mathbf{h}}_{2,j}^H \right) \\
\mathbf{Q}_n &= \bar{\mathbf{h}}_{2,n} \bar{\mathbf{h}}_{1,n}^H \left(\sum_{j=1, j \neq n}^{N_{\text{IRS}}} \phi_j^* \bar{\mathbf{h}}_{1,j} \bar{\mathbf{h}}_{2,j}^H \right),
\end{aligned} \tag{50}$$

Through the above discussion, both \mathbf{P}_n and \mathbf{Q}_n are independent of ϕ_n . Under this condition, the multiple variable optimization problem (45) can be converted into single variable optimization problem (49). Therefore, with respect to ϕ_n , the optimization objective can be formulated as

$$\begin{aligned}
\phi_n^{\text{opt}} &= \arg \max_{\phi_n} \log_2 \left| \frac{\rho}{\delta^2 N_s} (\mathbf{P}_n + \phi_n \mathbf{Q}_n + \phi_n^* \mathbf{Q}_n^H) \right| \\
s.t. \quad &\phi_n = \bar{\mu} e^{j\varphi_n}, \varphi_n \in \mathcal{F}.
\end{aligned} \tag{51}$$

Nevertheless, due to the discrete phase shift φ_n , this single variable optimization problem (51) is still non-convex. One may note that the discrete phase shift φ_n is selected from a predefined phase shift set \mathcal{F} and is finite. Hence, the non-convex optimization problem can be considered as a phase shift search problem. The detailed process of our proposed linear search algorithm is illustrated in **Algorithm 3**.

Algorithm 3 Linear Search Algorithm

Require: $\mathbf{H}_1, \mathbf{H}_2, \mathbf{F}, \mathbf{W}, b, \varphi_{\max}, \mathcal{F}$,

 1: Initialize the phase shift matrix $\Phi = (\phi_1, \phi_2, \dots, \phi_{N_{\text{IRS}}})$,

 2: **Iterative Process:**

 3: **for** $n = 1 : N_{\text{IRS}}$ **do**

 4: **for all** $\varphi_n \in \mathcal{F}$ **do**

 5: Calculate \mathbf{P}_n and \mathbf{Q}_n based on (50),

 6: Obtain the optimal ϕ_n^{opt} according to (51),

 7: Update the n th entry of Φ : $\phi_n = \phi_n^{\text{opt}}$,

 8: **end for**

 9: **end for**
Ensure: $\Phi^{\text{opt}} = \text{diag}(\phi_1^{\text{opt}}, \phi_2^{\text{opt}}, \dots, \phi_{N_{\text{IRS}}}^{\text{opt}})$

VI. SIMULATION RESULTS

In this section, simulation results are provided to examine the effectiveness of the considered algorithms for the downlink IRS-enabled THz MIMO system, including random phase algorithm, C-GD algorithm, A-GD algorithm and AO algorithm. In addition, to demonstrate the performance improvement brought by the IRS, the conventional THz MIMO system without the IRS is also simulated under the same simulation conditions as the IRS-enabled system. The working frequency of each IRS element is at $f = 1.6$ THz and the maximum phase response is $\varphi_{\max} = 306.82^\circ$. In this scenario, the distance of BS-IRS, IRS-MS and BS-MS is set as $\bar{r}_0 = 10$ m, $\tilde{r}_0 = 10$ m, and $r_0 = 16$ m, respectively. The LOS path of BS-MS link is blocked by the obstacle, and thus the NLOS paths are assisted by the IRS. Considering the sparse nature of THz channel, we assume that the BS-IRS channel \mathbf{H}_1 contains $L_1 = 3$ propagation paths, such as one LOS path and two NLOS paths. More specifically, the complex gain of LOS path is generated based on (9) and the complex gains of NLOS paths are computed by (11). The molecular absorbing coefficient and the reflection coefficient of ceramic tile are set as $\kappa(f) = 0.2$ and $\xi(f) = 10^{-6}$ [26]. Similarly, the parameter settings of the IRS-MS channel \mathbf{H}_2 are consistent with the channel \mathbf{H}_1 . The number of the RF chains at the BS and the MS is set as $M_{\text{BS}} = 6$ and $M_{\text{MS}} = 4$. To combat the serious attenuation, the antenna gains are configured as $G_t = G_r = 55$ dBi. Here we define the signal-to-noise ratio (SNR) as $\text{SNR} = \rho/\sigma^2$, and all simulation results

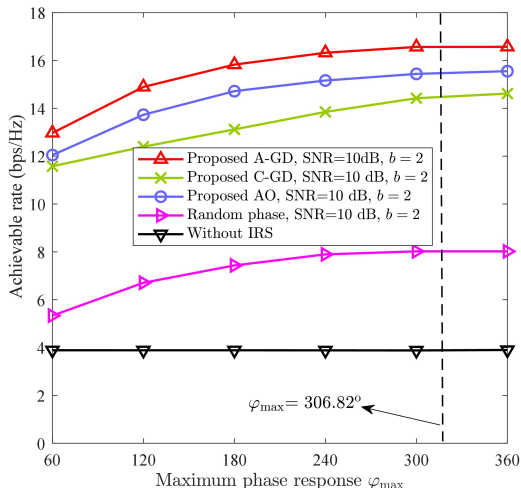


Fig. 5: Achievable rate comparisons of considered algorithms versus φ_{\max} .

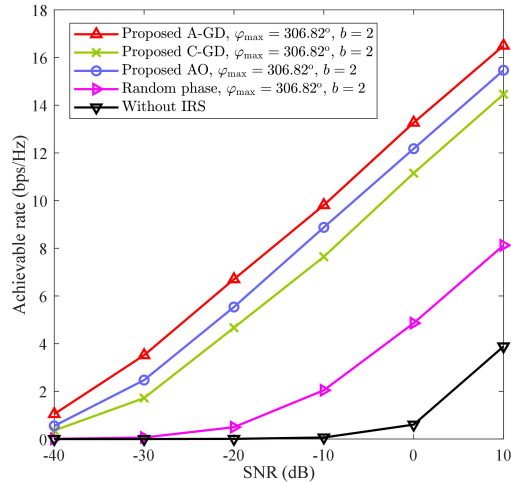


Fig. 6: Achievable rate comparisons of considered algorithms versus SNR.

are averaged over 1000 random channel realizations.

A. Achievable Rates Analysis

Fig. 5 investigates the achievable rate performance with the increasing number of the maximum phase response φ_{\max} , which aims to validate the effectiveness of the proposed hardware architecture mentioned in Section II. The parameters of the THz MIMO system are set as $N_{\text{BS}} = 512$, $N_{\text{IRS}} = 128$, $N_{\text{MS}} = 32$. From Fig. 5 we can note that the achievable rate of each IRS-enabled scheme improves firstly and then converges to a fixed value. Remarkably, the achievable rates of our proposed algorithms with $\varphi_{\max} = 306.82^\circ$ have already converged, and possess the same performance as the ideal case with $\varphi_{\text{ideal}} = 360^\circ$. Compared with low phase response $\varphi_{\max} = 60^\circ$, the considered A-GD algorithm, C-GD algorithm, AO algorithm and the random phase scheme with designed phase response $\varphi_{\max} = 306.82^\circ$ realize the achievable rate enhancement of 3.59 bps/Hz, 3.50 bps/Hz, 2.79 bps/Hz and 2.68 bps/Hz, respectively. Hence, the numerical results verify the efficient hardware structure of the graphene-based IRS.

Fig. 6 depicts the achievable rate performance versus diverse SNR values in the THz MIMO system with $N_{\text{BS}} = 512$, $N_{\text{IRS}} = 128$, $N_{\text{MS}} = 32$. Obviously, the achievable rate of the IRS-enabled THz MIMO system greatly outperforms the conventional THz system without IRS that can hardly meet communication requirements. In addition, compared with random phase scheme, our developed data rate optimization schemes (e.g., A-GD, C-GD, AO) is able to achieve the

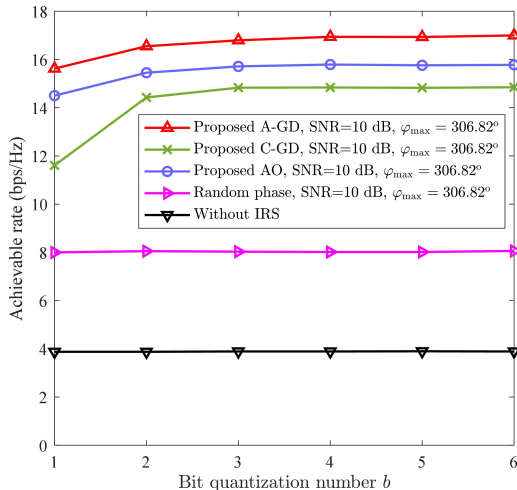


Fig. 7: Achievable rate comparisons of considered algorithms versus b .

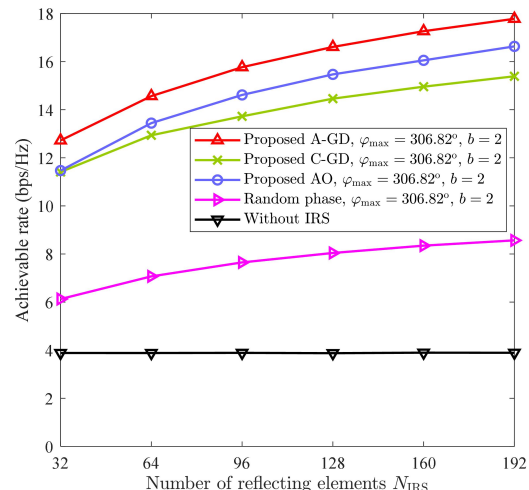


Fig. 8: Achievable rate comparisons of considered algorithms versus N_{IRS} .

performance improvement by a large margin, which reveals the necessity of capacity analysis. Numerically, under the condition of SNR=10 dB, the performance gap between the random phase scheme and the THz system without IRS is about 4.24 bps/Hz. Meanwhile, the achievable rates of A-GD algorithm, AO algorithm and C-GD algorithm are around 8.4 bps/Hz, 7.35 bps/Hz and 6.34 bps/Hz higher than the random phase scheme, respectively. Thus, our proposed optimization algorithms can be employed to enhance the communication rate for the IRS-assisted THz MIMO systems.

Fig. 7 provides the achievable rate performance versus the different number of bit quantization for the THz system with $N_{\text{BS}}=512$, $N_{\text{IRS}}=128$, $N_{\text{MS}}=32$. Fig. 7 indicates that the achievable rates of both the random phase scheme and the conventional THz system without IRS are insensitive to the number of bit quantization. Instead, our proposed data rate optimization algorithms are evidently affected by the quantization resolution of reflecting elements. In the case of $b=1$, all the developed algorithms (e.g., A-GD, C-GD, AO) suffer from the obvious performance degradation due to the limited quantization precision of the discrete phase shifts. Specifically, in contrast with $b=2$, the proposed A-GD algorithm, C-GD algorithm and AO algorithm with $b=1$ endure about 0.93 bps/Hz, 2.82 bps/Hz and 0.95 performance penalty, respectively. Intriguingly, the achievable rates of our proposed algorithms with $b=2$ almost yields the similar performance compared with $b \geq 3$, indicating that $b=2$ is sufficient to quantize the discrete phase shifts of the IRS elements in practice.

Fig. 8 discusses the achievable rate comparisons of considered schemes versus the number of the IRS elements N_{IRS} for the THz system configured as $N_{\text{BS}}=512$ and $N_{\text{MS}}=32$. From Fig. 8 we can note that the achievable rate of the THz system without IRS inherits the worst performance due to the lack of installing the IRS, and remains unchanged along with the diverse values of N_{IRS} . In terms of these IRS-enabled schemes, our developed achievable rate optimization algorithms (e.g., A-GD, C-GD, AO) outstrip the random phase scheme. More importantly, when the number of reflecting elements increases, the performance gap between our proposed algorithms and the random phase scheme become much larger accordingly. Under the condition of $N_{\text{IRS}}=192$, our developed A-GD, C-GD and AO algorithms are able to achieve around 9.21 bps/Hz, 6.82 bps/Hz and 8.06 bps/Hz performance enhancement compared with the random phase scheme. Hence, except for the performance gain brought by the IRS, our proposed optimization algorithms can also be leveraged to further improve the achievable rate of the IRS enabled THz MIMO system.

B. Complexity Analysis

In this subsection, the complexity of our considered algorithms is analyzed in detail, and the complexity represents the total number of the complex multiplications. We first analyze the complexity of the AO algorithm that is the combination of the CBC algorithm and the linear search algorithm. In terms of the CBC algorithm, the complexity for *Case 1* is $\mathcal{O}(N_{\text{BS}}N_s)$ while the complexity for the *Case 2* is $\mathcal{O}(N_{\text{BS}}M_{\text{BS}}N_s + 2N_{\text{BS}}N_s + N_{\text{BS}})$. Hence, the maximum complexity for precoding problem equals to the complexity of *Case 2*. Similarly, for combining problem, the complexity is $\mathcal{O}(N_{\text{MS}}N_s + N_{\text{MS}})$. To sum up, the overall complexity of the CBC algorithm can be expressed as

$$\mathcal{O}\left(N_{\text{BS}}M_{\text{BS}}N_s + 2N_{\text{BS}}N_s + N_{\text{BS}} + N_{\text{MS}}N_s + N_{\text{MS}}\right), \quad (52)$$

For the linear search algorithm, there are total $\mathcal{O}(N_{\text{IRS}}2^b)$ possible phase shift combinations, and the complexity of calculating each ϕ_n is $\mathcal{O}(2N_{\text{IRS}}N_s^2 + N_s^3)$. Thus, the complexity of the linear search algorithm can be written as

$$\mathcal{O}\left(2^{b+1}N_{\text{IRS}}^2N_s^2 + 2^bN_{\text{IRS}}N_s^3\right), \quad (53)$$

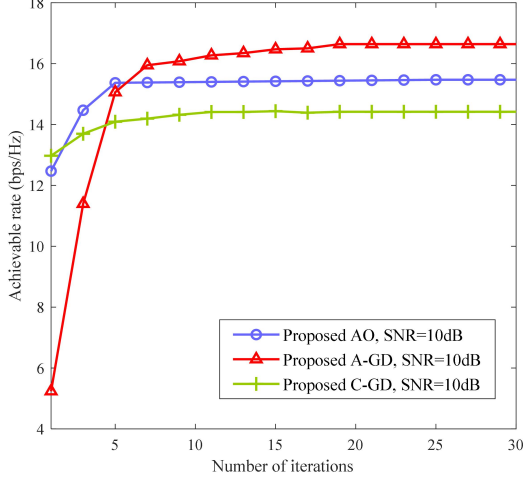


Fig. 9: Convergence comparisons of our proposed algorithms versus the number of iterations.

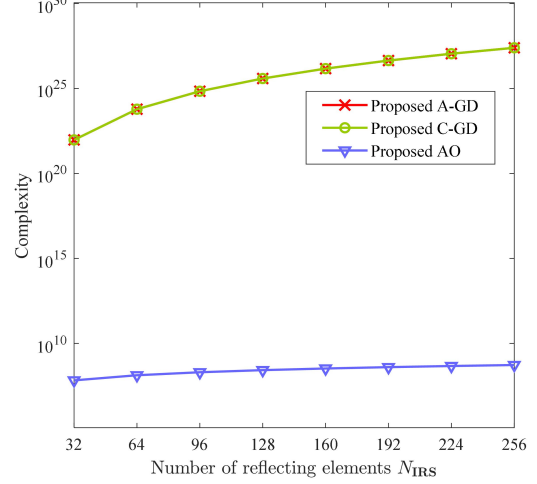


Fig. 10: Complexity comparisons of our proposed algorithms versus N_{IRS} .

Based on (52) and (53), the complexity of the AO algorithm with I_o iterations is written as

$$\mathcal{O}_{\text{AO}} \left[I_o \left(\begin{array}{l} N_{\text{BS}} M_{\text{BS}} N_s + 2N_{\text{BS}} N_s + N_{\text{BS}} \\ + N_{\text{MS}} N_s + N_{\text{MS}} \\ + 2^{b+1} N_{\text{IRS}}^2 N_s^2 + 2^b N_{\text{IRS}} N_s^3 \end{array} \right) \right], \quad (54)$$

For the C-GD algorithm, the complexity of initializing $\mathbf{A} = -(\mathbf{H}_1^T \otimes \mathbf{H}_2)^H (\mathbf{H}_1^T \otimes \mathbf{H}_2)$ is $\mathcal{O}(2N_{\text{BS}}^3 N_{\text{MS}}^3 N_{\text{IRS}}^6)$. On the other hand, the complexity of computing $\nabla_{\varphi} f(\varphi)$ is $\mathcal{O}(N_{\text{IRS}}^2)$. Thus, the complexity of the C-GD algorithm with maximum number of iterations I_c can be expressed as

$$\mathcal{O}_{\text{C-GD}} (I_c N_{\text{IRS}}^2 + 2N_{\text{BS}}^3 N_{\text{MS}}^3 N_{\text{IRS}}^6), \quad (55)$$

Next, the A-GD algorithm needs to calculate the adaptive step size for each iteration process and the complexity of calculating λ^i is $\mathcal{O}(3N_{\text{IRS}}^2/2)$. Thus, the overall complexity of the A-GD algorithm with the maximum number of iterations I_a can be written as

$$\mathcal{O}_{\text{A-GD}} \left(\frac{5}{2} I_a N_{\text{IRS}}^2 + 2N_{\text{BS}}^3 N_{\text{MS}}^3 N_{\text{IRS}}^6 \right), \quad (56)$$

Fig. 9 depicts the convergence behavior of our proposed algorithms for the THz MIMO system with $N_{\text{BS}} = 512$ and $N_{\text{MS}} = 32$. From Fig. 9 we can know that the converged number of iterations for the A-GD algorithm, the C-GD algorithm and the AO algorithm is $I_a = 20$, $I_c = 20$ and $I_o = 3$, respectively. Based on the convergence analysis, the complexity of our

proposed algorithms along with the number of reflecting elements N_{IRS} is compared in Fig. 10. As shown in Fig. 10, the proposed AO algorithm has the lowest complexity. Instead, the A-GD algorithm and the C-GD algorithm suffer from abundant calculation burden. In addition, when N_{IRS} increases, the complexity of AO algorithm changes slowly while the A-GD and the C-GD algorithms grows rapidly. In the case of $N_{\text{IRS}} = 128$, the complexity of the AO, C-GD and A-GD is around 2.68×10^8 , 2.87×10^{25} and 2.87×10^{25} , respectively. By observing Fig. 6 and Fig. 10, the AO algorithm realizes a better compromise between the achievable rate performance and computational complexity.

VII. CONCLUSION

This paper jointly considers the hardware structure and the capacity analysis for the IRS-enabled THz MIMO communications. To care to the practical working effects of the IRS, we primarily probe into the characteristics of the graphene-based IRS, including the phase response and the reflection amplitude. According to the hard design, the C-GD algorithm and the A-GD algorithm is developed to settle the data rate optimization problem, where the A-GD algorithm owns much better achievable rate compared with the C-GD algorithm. Furthermore, in order to depress the complexity of the gradient descent based methods, an AO algorithm by alternately executing the CBC algorithm and the linear search algorithm, which makes a better trade-off between complexity and data rate performance. In the near future, our research work will concentrate on the practical measurements for the IRS enabled THz communications.

REFERENCES

- [1] K. B. Letaief, W. Chen, Y. Shi, et al., "The Roadmap to 6G: AI Empowered Wireless Networks," *IEEE Commun. Mag.*, vol. 57, no. 8, pp. 84-90, Aug. 2019.
- [2] X. You et al., "Towards 6G wireless communication networks: vision, enabling technologies, and new paradigm shifts," *Sci. China Inf. Sci.*, vol. 64, no. 1, Jan. 2021, doi: 10.1007/s11432-020-2955-6.
- [3] Z. Chen, X. Y. Ma, B. Zhang, et al., "A survey on terahertz communications," *China Commun.*, vol. 16, no. 2, pp. 1-35, Feb. 2019.
- [4] I. F. Akyildiz, J. M. Jornet, and C. Han, "Terahertz band: Next frontier for wireless communications," *Phys. Commun. (Elsevier)*, vol. 12, no. 4, pp. 16-32, 2014.
- [5] R. Piesiewicz et al., "Short-Range Ultra-Broadband Terahertz Communications: Concepts and Perspectives," *IEEE Antennas Propag. Mag.*, vol. 49, no. 6, pp. 24-39, Dec. 2007.
- [6] I. F. Akyildiz, C. Han and S. Nie, "Combating the Distance Problem in the Millimeter Wave and Terahertz Frequency Bands," *IEEE Commun. Mag.*, vol. 56, no. 6, pp. 102-108, June. 2018.

- [7] C. Han and Y. Chen, "Propagation Modeling for Wireless Communications in the Terahertz Band," *IEEE Commun. Mag.*, vol. 56, no. 6, pp. 96-101, Jun. 2018.
- [8] T. Cui, M. Qi, X. Wan, et al., "Coding metamaterials, digital metamaterials and programmable metamaterials," *Light Sci. Appl.*, vol. 3, pp. e218, 2014.
- [9] C. Liaskos, S. Nie, A. Tsioliaridou, A. Pitsillides, S. Ioannidis and I. Akyildiz, "A New Wireless Communication Paradigm through SoftwareControlled Metasurfaces," *IEEE Commun. Mag.*, vol. 56, no. 9, pp. 162-169, Sept. 2018.
- [10] C. Huang, A. Zappone, G. C. Alexandropoulos, et al., "Reconfigurable Intelligent Surfaces for Energy Efficiency in Wireless Communication," *IEEE Trans. Wirel. Commun.*, vol. 18, no. 8, pp. 4157-4170, Aug. 2019.
- [11] X. Ma, Z. Chen, W. Chen, et al., "Joint Channel Estimation and Data Rate Maximization for Intelligent Reflecting Surface Assisted Terahertz MIMO Communication Systems," *IEEE Access*, vol. 8, pp. 99565-99581, May 2020.
- [12] Q. Wu and R. Zhang, "Intelligent Reflecting Surface Enhanced Wireless Network via Joint Active and Passive Beamforming," *IEEE Trans. Wirel. Commun.*, vol. 18, no. 11, pp. 5394-5409, Nov. 2019.
- [13] X. Ma, Z. Chen, W. Chen, et al., "Intelligent Reflecting Surface Enhanced Indoor Terahertz Communication Systems," *Nano Commun. Netw.*, vol. 24, pp. 100284, May. 2020.
- [14] H. Shen, W. Xu, S. Gong, Z. He and C. Zhao, "Secrecy Rate Maximization for Intelligent Reflecting Surface Assisted Multi-Antenna Communications," *IEEE Commun. Lett.*, vol. 23, no. 9, pp. 1488-1492, Sept. 2019.
- [15] S. Zhang and R. Zhang, "Capacity Characterization for Intelligent Reflecting Surface Aided MIMO Communication," *IEEE J. Sel. Areas Commun.*, vol. 38, no. 8, pp. 1823-1838, Aug. 2020.
- [16] A. Goldsmith, S. A. Jafar, N. Jindal and S. Vishwanath, "Capacity limits of MIMO channels," *IEEE J. Sel. Areas Commun.*, vol. 21, no. 5, pp. 684-702, Jun. 2003.
- [17] O. E. Ayach, S. Rajagopal, S. Abu-Surra, et al., "Spatially Sparse Precoding in Millimeter Wave MIMO Systems," *IEEE Trans. Wirel. Commun.*, vol. 13, no. 3, pp. 1499-1513, Mar. 2014.
- [18] H. Chen, A. J. Taylor, N. Yu, "A review of metasurfaces: physics and applications," *Rep. Prog. Phys.*, vol. 79, no. 7, pp. 076401, Jun. 2016.
- [19] H. Wong, D. Akinwande, "Carbon Nanotube and Graphene Device Physics," *Cambridge University Press*, 2010.
- [20] D. K. Efetov, P. Kim, "Controlling electron-phonon interactions in graphene at ultrahigh carrier densities," *Phys. Rev. Lett.*, vol. 105, no. 25, pp. 256805, Dec. 2010.
- [21] S. Lee, M. Choi, T. Kim et al., "Switching terahertz waves with gate-controlled active graphene metamaterials," *Nat. Mater.*, vol. 11, pp. 936-941, Sep. 2012.
- [22] Y. Yang, W. Wang, P. Moitra et al., "Dielectric Meta-Reflectarray for Broadband Linear Polarization Conversion and Optical Vortex Generation," *Nano Lett.*, vol.14, no.3, pp. 1394-1399, Feb. 2014.
- [23] A. Pors, S. I. Bozhevolnyi, "Plasmonic metasurfaces for efficient phase control in reflection," *Opt. Express*, vol. 21, no. 22, pp. 27438-27451, Nov. 2013.
- [24] Z. Li, K. Yao, F. Xia et al., "Graphene Plasmonic Metasurfaces to Steer Infrared Light," *Sci. Rep.*, vol. 5, no. 12423, Jul. 2015.
- [25] A. A. M. Saleh and R. Valenzuela, "A Statistical Model for Indoor Multipath Propagation," *IEEE J. Sel. Areas Commun.*, vol. 5, no. 2, pp. 128-137, Feb. 1987.
- [26] C. Han, A. O. Bicen, I. F. Akyildiz, "Multi-Ray Channel Modeling and Wideband Characterization for Wireless Communications in the Terahertz Band," *IEEE Trans. Wirel. Commun.*, vol. 14, no. 5, pp. 2402-2412, Dec. 2015.
- [27] S. Zegrar, L. Afeef, H. Arslan, "A General Framework for RIS-Aided mmWave Communication Networks: Channel Estimation and Mobile User Tracking," *arXiv*, Sept. 2020. [Online]. Available: <https://arxiv.org/abs/2009.01180>.

- [28] K. Ying, Z. Gao, S. Lyu, et al., "GMD-Based Hybrid Beamforming for Large Reconfigurable Intelligent Surface Assisted Millimeter-Wave Massive MIMO," *IEEE Access*, vol. 8, pp. 19530-19539, 2020.
- [29] X. Zhang, A. F. Molisch, and S.-Y. Kung, "Variable-phase-shift-based RF-baseband codesign for MIMO antenna selection," *IEEE Trans. Signal Process.*, vol. 53, no. 11, pp. 4091-4103, Nov. 2005.
- [30] C. Rusu, R. Mndez-Rial, N. Gonzlez-Prelcic, and R. W. Heath, "Low Complexity Hybrid Precoding Strategies for Millimeter Wave Communication Systems," *IEEE Trans. Wirel. Commun.*, vol. 15, no. 12, pp. 8380-8393, Dec. 2016.